AD-A079 919 STD RESEARCH CORP ARCADIA CALIF F/G 20/9
MAGNETOGASDYNAMIC PHENOMENA IN PULSED MHD FLOWS.(U)
OCT 79 D A OLIVER, T F SWEAN, D M MARKHAM N00014-77-C-0574
UNCLASSIFIED STD-UP-002-77-1 NL

1 OF 1
AD A079919

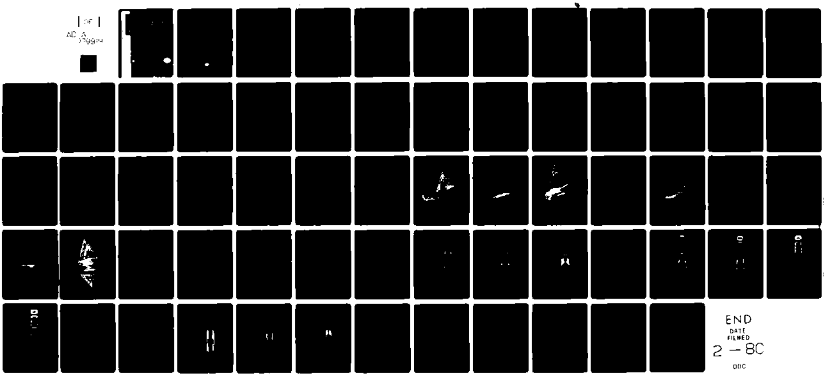

END
DATE FILMED
2 - 80
DDC

STD-UP-002-77-1
STDR-79-8

MAGNETOGASDYNAMIC PHENOMENA IN PULSED MHD FLOWS

D.A. OLIVER, T.F. SWEAN, Jr., D.M. MARKHAM,
C.D. BANGERTER, AND S.T. DEMETRIADES

OCTOBER 1979

~~INTERIM~~ SUMMARY REPORT
FOR THE PERIOD
1 OCTOBER 1978 THROUGH 30 SEPTEMBER 1979

STD RESEARCH CORPORATION
ARCADIA, CA 91006

PREPARED FOR THE
U.S. DEPARTMENT OF THE NAVY
OFFICE OF NAVAL RESEARCH
UNDER CONTRACT N00014-77-C-0574
WORK UNIT NR-099-415

STD-UP-002-77-1
STDR-79-8

MAGNETOGASDYNAMIC PHENOMENA IN PULSED MHD FLOWS

D.A. OLIVER, T.F. SWEAN, Jr., D.M. MARKHAM,
C.D. BANGERTER, AND S.T. DEMETRIADES

OCTOBER 1979

INTERIM SUMMARY REPORT
FOR THE PERIOD
1 OCTOBER 1978 THROUGH 30 SEPTEMBER 1979

STD RESEARCH CORPORATION
ARCADIA, CA 91006

PREPARED FOR THE
U.S. DEPARTMENT OF THE NAVY
OFFICE OF NAVAL RESEARCH
UNDER CONTRACT N00014-77-C-0574
WORK UNIT NR-099-415

SECURITY CLASSIFICATION OF THIS PAGE (When Data Entered)

REPORT DOCUMENTATION PAGE		READ INSTRUCTIONS BEFORE COMPLETING FORM
1. REPORT NUMBER STDR-79-8	2. GOVT ACCESSION NO.	3. RECIPIENT'S CATALOG NUMBER
4. TITLE (and Subtitle) Magnetogasdynamic Phenomena in Pulsed MHD Flows.		5. ~~TYPE OF REPORT & PERIOD COVERED~~ Annual Summary rept. 1 Oct 78-[redacted] 30 Sep[redacted] 79
		6. ~~PERFORMING ORG. REPORT NUMBER~~
7. AUTHOR(s) [redacted] A. Oliver, [redacted] F. Swean, Jr., D. M. Markham, C. D. Bangerter [redacted] S. T. Demetriades		8. CONTRACT OR GRANT NUMBER(s) N00014-77-C-0574
9. PERFORMING ORGANIZATION NAME AND ADDRESS STD Research Corporation		10. PROGRAM ELEMENT, PROJECT, TASK AREA & WORK UNIT NUMBERS NR 099-415
11. CONTROLLING OFFICE NAME AND ADDRESS U.S. Dept. of Navy Office of Naval Research Green Street, Pasadena, CA		12. ~~REPORT DATE~~ 1 Oct[redacted]79
		13. ~~NUMBER OF PAGES~~ 55
14. MONITORING AGENCY NAME & ADDRESS (if different from Controlling Office)		15. SECURITY CLASS. (of this report) Unclassified
		15a. DECLASSIFICATION/DOWNGRADING SCHEDULE
16. DISTRIBUTION STATEMENT (of this Report) Unlimited		
17. DISTRIBUTION STATEMENT (of the abstract entered in Block 20, if different from Report) Unlimited		
18. SUPPLEMENTARY NOTES		
19. KEY WORDS (Continue on reverse side if necessary and identify by block number) Magnetohydrodynamic Flow, High Magnetic Reynolds Number Flow, Pulsed MHD Flows.		

6 10 David Thomas 9 15 11 12 66

DISTRIBUTION STATEMENT A
Approved for public release;
Distribution Unlimited

14 STD-UP-002-77-1, STDR-79-8

20. ABSTRACT (Continue on reverse side if necessary and identify by block number)

A summary of progress made in the prediction of magnetogasdynamic phenomena in explosion MHD flows. Theoretical and computational results are presented for quasi-one-dimensional and two-dimensional high Reynolds number flows in both weak and strong MHD interaction.

400 046 GM

DD FORM 1 JAN 73 1473 EDITION OF 1 NOV 65 IS OBSOLETE
S/N 0102 LF 014 6601

SECURITY CLASSIFICATION OF THIS PAGE (When Data Entered)

TABLE OF CONTENTS

TABLE OF CONTENTS ii

LIST OF FIGURES iii

LIST OF TABLES v

1.0 INTRODUCTION 1

2.0 THE MATHEMATICAL DESCRIPTION OF MAGNETO-GASDYNAMIC FLOWS 2

2.1 Fluid Conservation Laws 2

2.2 The Electromagnetic Contributions 3

2.3 Fluid-Electrical System 6

2.4 Viscous and Heat Conduction Effects 8

2.5 Nondimensional Forms 9

2.6 Applied and Induced Fields 14

3.0 QUASI-ONE-DIMENSIONAL TRANSIENT MAGNETO-GASDYNAMICS OF HYPERVELOCITY PULSED FLOWS 15

3.1 Plasma Flow Configuration 15

3.2 The One-Dimensional Description 19

3.3 Interaction at Low Magnetic Reynolds Number 24

3.4 Interaction at High Magnetic Reynolds Number 26

3.5 Transitional Plasmoids 32

3.6 Summary Remarks 36

4.0 CURRENT AND MAGNETIC FIELDS IN TWO-DIMENSIONAL HIGH MAGNETIC REYNOLDS NUMBER FLOWS WITH NON-UNIFORM VELOCITY AND ELECTRICAL CONDUCTIVITY 38

4.1 Channel and Applied Magnetic Field Configuration 38

4.2 Two-Dimensional Electrical Description 39

4.3 Uniform Velocity and Electrical Conductivity 40

4.3.1 Load with Point Electrode 40
4.3.2 Load with Finite Electrode 40

4.4 Nonuniform Velocity and Conductivity Distributions Resulting from a Shock System 44

4.4.1 Shock in Front of Electrodes 44
4.4.2 Shock in Channel Center 44
4.4.3 Shock at Upstream Edge of Magnetic Field 44

4.5 Nonuniform Velocity and Conductivity Distributions Resulting from Supersonic Boundary Layers on the Walls of the MHD Generator Duct 44

4.5.1 Flow Structure for Electrical Interaction 44
4.5.2 Electrical Conduction at Vanishing Magnetic Reynolds Number 50
4.5.3 Electrical Conduction at High Magnetic Reynolds Number 50

REFERENCES 54

LIST OF FIGURES

Fig. 3-1.	Schematic of explosion driven plasmoid flow	16
Fig. 3-2.	Space-time diagram of strong interaction hypervelocity plasmoids	16
Fig. 3-3.	Initial condition for plasmoid interaction for the pressure, temperature, and velocity	23
Fig. 3-4.	Velocity field of plasmoid in transit through an applied magnetic field under strong interaction (I = 20), low magnetic Reynolds number ($R_m = 0.1$) conditions	27
Fig. 3-5.	Current density distribution for conditions of Fig. 3-4	28
Fig. 3-6.	Temperature distribution for conditions of Fig. 3-4	29
Fig. 3-7.	Current distribution for a strong interaction plasmoid at $R_m = 5$	30
Fig. 3-8.	Velocity distribution for a transitional plasmoid	31
Fig. 3-9.	Current distribution for transitional plasmoid of Fig. 3-8	34
Fig. 3-10.	Temperature field corresponding to Figs. 3-8, 3-9, showing developing electrothermal instability	35
Fig. 4-1.	Induced magnetic field isolevels in high magnetic Reynolds number flow. Uniform velocity and conductivity: point electrode	41
Fig. 4-2.	Induced magnetic field isolevels in high magnetic Reynolds number flow. Uniform velocity and conductivity: finite electrode	42
Fig. 4-3.	Induced magnetic field isolevels in high magnetic Reynolds number flow. As in Fig. 4-2 but $\tilde{I} = 1$	43
Fig. 4-4.	Induced magnetic field isolevels in high magnetic Reynolds number flow. Shock system present with $(\ )_1$ denoting upstream and $(\ )_2$ denoting downstream conditions	45
Fig. 4-5.	Induced magnetic field isolevels in high magnetic Reynolds number flow. As in Fig. 4-4, but conductivity jump of 10; downstream eddy cell structure influenced by zero current flow boundary condition at duct exit	46
Fig. 4-6.	Induced magnetic field isolevels in high magnetic Reynolds number flow. As in Fig. 4-5, but with a velocity jump of 1/2	47

List of Figures (cont'd)

Fig. 4-7. Induced magnetic field isolevels in high magnetic Reynolds number flow. Conductivity jump of 10 and shock system moved into channel center 48

Fig. 4-8. Induced magnetic field isolevels in high magnetic Reynolds number flow. Conductivity jump of 10 and shock system moved upstream to magnetic field edge 51

Fig. 4-9. Induced magnetic field isolevels under conditions of low magnetic Reynolds number flow ($R_M = 0.01$) and velocity and conductivity nonuniformities resulting from supersonic boundary layer development through the duct 52

Fig. 4-10. Induced magnetic isolevels for high magnetic Reynolds number flow ($R_M = 7.13$) and velocity and conductivity nonuniformities resulting from supersonic boundary layer development through the duct 53

LIST OF TABLES

Table I.	Conditions for Interaction at Low Magnetic Reynolds Number	25
Table II.	Conditions for Interaction at High Magnetic Reynolds Number	25
Table III.	Conditions for Transitional Plasmoid	25

1. INTRODUCTION

This work is aimed at the understanding, description, and prediction of magnetohydrodynamic phenomena exhibited under conditions of extremely high interaction and large magnetic Reynolds number. The plasmas which consistute the fluid medium in such flows may exhibit nonideal thermodynamic and kinetic behavior. The theoretical work at ~~STD Research~~ under ONR ~~support~~ has two principal objectives: ~~(1)~~ the elucidation of basic phenomena in strong interaction high magnetic Reynolds number flows independently of specific experiments or machines; and ~~(2)~~ the perfection of predictive theories to accurately describe and model specific experiments aimed at magnetohydrodynamic power production.

In what follows we present the general mathematical description of magnetogasdynamic flows in the high magnetic Reynolds number regime. We present several illustrative calculations of quasi-one-dimensional transient effects in strong interaction flows. ~~We then present~~ two-dimensional high Reynolds number electricity results are presented including the realistic effects of nonuniform velocity and electrical conductivity resulting from hypersonic boundary layers and from shock-induced nonuniformities.

2. THE MATHEMATICAL DESCRIPTION OF MAGNETOGASDYNAMIC FLOWS

2.1 Fluid Conservation Laws

We may describe the fluid in terms of its mass density, ρ, velocity $\vec{U}$, and internal energy ϵ. We describe the electromagnetic effects in terms of the electric field $\vec{E}$ and magnetic field $\vec{B}$. These variables are considered to be general functions of space $\vec{x}$ and time t. The conservation laws for mass, momentum, and energy are

$$\frac{\partial \rho}{\partial t} + \nabla \cdot (\rho \vec{U}) = 0 \tag{1}$$

$$\frac{\partial}{\partial t}(\rho \vec{U}) + \nabla \cdot (\rho \vec{U}\vec{U}) = \nabla \cdot \overleftrightarrow{\pi} + \vec{J} \times \vec{B} \tag{2}$$

$$\frac{\partial}{\partial t}\left[\rho\left(\epsilon + U^2/2\right)\right] + \nabla \cdot \left[\left(\epsilon + U^2/2\right)\rho\vec{U}\right] = \nabla \cdot \left(\overleftrightarrow{\pi} \cdot \vec{U}\right) - \nabla \cdot \vec{q} + \vec{J} \cdot \vec{E} \tag{3}$$

In the conservation laws, $\overleftrightarrow{\pi}$ is the total pressure tensor and $\vec{q}$ is the heat flux vector. This system of conservation laws is completed in the limit of infinitely fast kinetics by the kinetic and caloric equations of state

$$p = p(\rho, \epsilon) \tag{4}$$

$$\epsilon = \epsilon(p, T) \tag{5}$$

where p is the isotropic part of the stress tensor $\overleftrightarrow{\pi}$ and T is the temperature. For a general fluid the state equations, Eqs. (4), (5) cannot be explicitly given but are embedded in the general statistical mechanical description of the equilibrium thermochemistry of the system.

In the case of a perfect gas with particular gas constant R and specific heat ratio γ explicit formulae may be given:

$$p = \rho R T \tag{6}$$

$$\epsilon = (\gamma - 1)^{-1} R T \tag{7}$$

$$p = \rho(\gamma - 1)\epsilon \tag{8}$$

2.2 The Electromagnetic Contributions

The electrical equations (consisting of the Maxwell equations and the generalized Ohm's law) govern the electric and magnetic fields $\vec{E}, \vec{B}$ and the conduction current density $\vec{J}$. In the hydromagnetic limit these are

$$\nabla \times \vec{E} = -\frac{\partial \vec{B}}{\partial t} \tag{9}$$

$$\nabla \times \vec{B} = \mu_0 \vec{J} \tag{10}$$

$$\nabla \cdot \vec{B} = 0 \tag{11}$$

$$\vec{J} = \sigma\left(\vec{E} + \vec{U} \times \vec{B}\right) + \vec{J}_K \tag{12}$$

where $\vec{J}_K$ is the thermal diffusion flux vector,

$$\vec{J}_K = \sigma \vec{K}$$

and $\vec{K}$ is given by [1]

$$\begin{aligned}\vec{K} \equiv -\Big[&\theta^{(1)} \nabla T_e + \theta^{(2)} \nabla T_e \times \vec{B} + \theta^{(3)} (\nabla T_e \times \vec{B}) \times \vec{B} \\ &- \sum_{\alpha=1}^{N} \Big[\beta_\alpha^{(1)} \nabla p_\alpha + \beta_\alpha^{(2)} \nabla p_a \times \vec{B} + \beta_\alpha^{(3)} (\nabla p_\alpha \times \vec{B}) \times \vec{B} \Big]\end{aligned} \tag{13}$$

The $\theta^{(1)}, \cdots$ and $\beta_\alpha^{(1)} \cdots$ are transport coefficients defined in [1], T_e is the electron temperature and the subscript α denotes a plasma component.

The contributions to the momentum and energy of the system by the electromagnetic field are contained within the Lorentz force, $\vec{J} \times \vec{B}$ and the Lorentz power $\vec{J} \cdot \vec{E}$. The Lorentz force may be represented in terms of the Maxwell stress tensor $\overleftrightarrow{T}$ as

$$\vec{J} \times \vec{B} = \nabla \cdot \overleftrightarrow{T} \tag{14}$$

where the Maxwell stress tensor is defined as

$$\overleftrightarrow{T} = \hat{\mu}_0^{-1} \left(\vec{B}\,\vec{B} - B^2/2\, \overleftrightarrow{I} \right) \tag{15}$$

Correspondingly the Lorentz power may be represented in terms of the Poynting flux $\vec{S}$ and the electromagnetic energy density e_m

$$\vec{J} \cdot \vec{E} = -\nabla \cdot \vec{S} - \frac{\partial e_m}{\partial t} \tag{16}$$

The Poynting flux $\vec{S}$ is defined as

$$\vec{S} = \hat{\mu}_0^{-1}\, \vec{E} \times \vec{B} \tag{17}$$

while the electromagnetic energy density is

$$e_m = \hat{\mu}_0^{-1}\, B^2/2 \tag{18}$$

Let us expand the Poynting flux in terms of $\vec{J}, \vec{B}$ through the use of the Ohm's law

$$\vec{J} = \sigma \left(\vec{E} + \vec{U} \times \vec{B} + \vec{K} \right)$$

We have

$$\vec{S} = \hat{\mu}_0^{-1}\left(\vec{E}\times\vec{B}\right) = \left(\hat{\mu}_0\sigma\right)^{-1}\vec{J}\times\vec{B} - \hat{\mu}_0^{-1}\left(\vec{U}\times\vec{B}\right)\times\vec{B} - \hat{\mu}_0^{-1}\vec{K}\times\vec{B}$$

The term $\vec{J}\times\vec{B}$ is simply $\nabla\cdot\overleftrightarrow{T}$. The term $(\vec{U}\times\vec{E})\times\vec{B}$ is readily shown to be

$$(\vec{U}\times\vec{B})\times\vec{B} = \vec{U}\cdot(\vec{B}\,\vec{B}) - \vec{U}\,(\vec{B}\cdot\vec{B})$$

which can be rearranged to

$$(\vec{U}\times\vec{B})\times\vec{B} = \vec{U}\cdot(\vec{B}\,\vec{B} - B^2/2\overleftrightarrow{I}) - \vec{U}\,(B^2/2)$$

The Poynting flux is therefore represented as

$$\vec{S} = e_m\vec{U} - \vec{U}\cdot\overleftrightarrow{T} + \eta\nabla\cdot\overleftrightarrow{T} - \eta\vec{J}_K\times\vec{B} \tag{19}$$

where $\eta \equiv (\hat{\mu}_0\sigma)^{-1}$ is the magnetic diffusivity. We note that the Poynting flux can be decomposed into four constituent parts: (a) a purely convected flux of electromagnetic energy carried by the motion of the medium ($e_m\vec{U}$); (b) a power flow represented by work done per unit time by the Maxwell stresses acting on the moving medium $-\vec{U}\cdot\overleftrightarrow{T}$; (c) a diffusive flux of electromagnetic energy driven by gradients of the Maxwell stress tensor ($+\eta\nabla\cdot\overleftrightarrow{T}$); and (d) a power flow represented by work done per unit time by the thermal diffusion flux ($-\eta\vec{J}_K\times\vec{B}$).

The electric and magnetic fields and currents may be expressed in terms of vecter potentials $\vec{A}$ and scalar potential Φ as

$$\vec{B} = \nabla\times\vec{A} \tag{20a}$$

$$\vec{E} = -\nabla\Phi - \frac{\partial\vec{A}}{\partial t} \tag{20b}$$

2.3 Fluid-Electrical System

The mass, momentum, and energy equations for the general, viscous, hydromagnetic system may now be expressed as

$$\frac{\partial \rho}{\partial t} + \nabla \cdot \vec{M} = 0 \tag{21}$$

$$\frac{\partial \vec{M}}{\partial t} + \nabla \cdot \overleftrightarrow{\Gamma} = \nabla \cdot \overleftrightarrow{\tau} \tag{22}$$

$$\frac{\partial e}{\partial t} + \nabla \cdot \vec{H} = \nabla \cdot (\vec{U} \cdot \overleftrightarrow{\tau}) - \nabla \cdot (\eta \nabla \cdot \overleftrightarrow{T}) - \nabla \cdot \vec{q} + \nabla \cdot (\eta \vec{J}_K \times \vec{B} \tag{23}$$

In the above $\vec{M} = \rho \vec{U}$ is the momentum density and $\overleftrightarrow{\Gamma}$ is the total fluid and electromagnetic momentum flux

$$\overleftrightarrow{\Gamma} = \rho \overrightarrow{UU} + p\overleftrightarrow{I} - \overleftrightarrow{T} \tag{24}$$

The total energy density is

$$e = \rho(\epsilon + U^2/2) + e_m \tag{25}$$

and $\vec{H}$ is the total enthalpy flux vector

$$\vec{H} = \left[(e + p)\overleftrightarrow{I} - \overleftrightarrow{T}\right] \cdot \vec{U} \tag{26}$$

The fluid stress tensor $\overleftrightarrow{\pi}$ has been decomposed into a pressure p and viscous stress tensor $\overleftrightarrow{\tau}$ where

$$p = -\frac{1}{3} \text{Trace } (\overleftrightarrow{\pi}) \tag{27}$$

and

$$\overleftrightarrow{\pi} = -p\overleftrightarrow{I} + \overleftrightarrow{\tau} \tag{28}$$

We may define the electromagnetic pressure p_m as the mean normal compressive Maxwell stress:

$$p_m = -\frac{1}{3}\,\mathrm{Trace}\,(\overleftrightarrow{T}) \tag{29}$$

Expressed in terms of the magnetic field intensity $\vec{B}$, the pressure is

$$p_m = \frac{1}{3}\left(B^2/2\hat{\mu}_0\right) \tag{30}$$

or expressed in terms of the electromagnetic energy density e_m

$$p_m = \frac{1}{3}\,e_m \tag{31}$$

The Maxwell stress tensor may be decomposed into a magnetic pressure p_m and a Maxwell stress deviator from isotropy $\overleftrightarrow{T}_*$ as

$$\overleftrightarrow{T} = \overleftrightarrow{T}_* - p_m\overleftrightarrow{I} \tag{32}$$

Equation (32) may be thought of as the defining equation for the Maxwell stress deviators $\overleftrightarrow{T}_*$. The mass, momentum, and energy equations may now be rewritten in alternative form as

$$\frac{\partial\rho}{\partial t} + \nabla\cdot\vec{M} = 0 \tag{33}$$

$$\frac{\partial\vec{M}}{\partial t} + \nabla\cdot\overleftrightarrow{G} = \nabla\cdot\overleftrightarrow{T}_* + \nabla\cdot\overleftrightarrow{\tau} \tag{34}$$

$$\frac{\partial e}{\partial t} + \nabla\cdot\vec{H} = \nabla\cdot(\vec{U}\cdot\overleftrightarrow{T}_*) + \nabla\cdot(\vec{U}\cdot\overleftrightarrow{\tau}) - \nabla\cdot\vec{q} - \nabla\cdot(\eta\nabla\cdot\overleftrightarrow{T}) + \nabla\cdot(\eta\vec{J}_K\times\vec{B}) \tag{35}$$

In the above, $\overleftrightarrow{G}$ is the total momentum flux with only the magnetic pressure included as the magnetic contribution

$$\overleftrightarrow{G} = \rho\vec{U}\vec{U} + (p + p_m)\overleftrightarrow{I} \tag{36}$$

while $\vec{H}$ is the total enthalpy flux consisting of both fluid and electromagnetic pressure and energy contributions.

$$\vec{H} = \left[e + (p + p_m)\right]\vec{U} \tag{37}$$

In terms of the total energy density e, the momentum density $\vec{M}$, and the electromagnetic energy density e_m, the state equations (6) - (8) become

$$p = (\gamma-1)\left[e - e_m - M^2/2\rho\right] \tag{38}$$

$$T = p/\rho R = \frac{(\gamma-1)}{\rho R}\left[e - e_m - M^2/2\rho\right] \tag{39}$$

Let us now consider the transformation of the electrical equations (9)-(12) into more useful forms. *Combining* Eqs. (9)-(12) we obtain the governing equation for the magnetic induction $\vec{B}$:

$$\frac{\partial \vec{B}}{\partial t} - \nabla \times (\vec{U} \times \vec{B}) = -\nabla \times (\eta \nabla \times \vec{B}) + \nabla \times \vec{K} \tag{40}$$

We note that given the magnetic induction $\vec{B}(\vec{x},t)$ governed by Eq. (40) one immediately has specified the Maxwell stress tensor $\overleftrightarrow{T}$ and the electromagnetic energy density e_m. Further, the current density $\vec{J}$ is determined from $\vec{B}$ as

$$\vec{J} = \hat{\mu}_0^{-1} \nabla \times \vec{B}$$

and the electric field $\vec{E}$ as

$$\vec{E} = -\vec{U} \times \vec{B} + \eta \nabla \times \vec{B} - \vec{K}$$

2.4 Viscous and Heat Conduction Effects

Let us now make some observations about the viscous stress tensor $\overleftrightarrow{\tau}$ and the heat flux vector $\vec{q}$. The Navier-Stokes moments of the Boltzmann equation yield kinetic theory forms of these quantities:

$$\overleftrightarrow{\tau}_L = 2\mu(\overleftrightarrow{\nabla U})_0 \tag{41}$$

$$\vec{q}_L = -\lambda \nabla T \tag{42}$$

In the above, μ and λ are the coefficients of viscosity and thermal conductivity and $(\overleftrightarrow{\nabla U})_0$ is the symmetrized, traceless velocity gradient tensor:

$$(\overleftrightarrow{\nabla U})_{0ij} \equiv \frac{1}{2}\left(\frac{\partial U_i}{\partial x_j} + \frac{\partial U_j}{\partial x_i}\right) - \frac{1}{3}\,\frac{\partial U_k}{\partial x_k}\,\delta_{ij}$$

We denote the stress tensor and heat flux vector with a subscript L to denote that these are laminar quantities. If, on the other hand, we interpret the fluid variables $\rho, \vec{U}, \epsilon, T, \cdots$ as <u>turbulent</u> <u>mean</u> quantities, then $\overleftrightarrow{\tau}$ and $\vec{q}$ contain turbulent contributions due to the turbulent velocity and enthalpy correlations. Hence, the complete stress and heat flux fields for a <u>turbulent</u> hydromagnetic medium are

$$\overleftrightarrow{\tau} = \langle \rho \vec{U}' \vec{U}' \rangle + \overleftrightarrow{\tau}_L$$

$$\vec{q} = \langle \rho \vec{U}' h' \rangle + \vec{q}_R + \vec{q}_L$$

where $\vec{U}', h'$ are the turbulently fluctuating velocity and enthalpy and $\langle\;\rangle$ denotes an ensemble average. A detailed higher order closure theory for the turbulent contributions $\langle \rho \vec{U}' \vec{U}' \rangle$, $\langle \rho \vec{U}' h' \rangle$ is given by Demetriades, Argyropoulos, and Lackner [2]. The radiative heat flux is $\vec{q}_R$. Since the optical depths in dense, explosion generated plasma are so small, the radiative heat flux is only important in layers near the plasma surface of the order of the radiation free path.

2.5 Nondimensional Forms

Let us consider the nondimensionalization of the fluid equations (33) - (35) and the electrical equation (4). For this purpose let us specify characteristic values of the variables as $\rho_0, U_0, \epsilon_0, p_0, T_0, \cdots$ as well as magnetic field B_0. We define a characteristic length L and characteristic time $t_0 = L/U_0$. We indicate nondimensional variables with $(\tilde{\ })$.

The fluid and electrical conservation laws then become

$$\frac{\partial\tilde{\rho}}{\partial\tilde{t}} + \tilde{\nabla}\cdot\vec{\tilde{M}} = 0 \tag{43}$$

$$\frac{\partial\vec{\tilde{M}}}{\partial\tilde{t}} + \tilde{\nabla}\cdot\overleftrightarrow{\tilde{\Gamma}} = R_e^{-1}\tilde{\nabla}\cdot\left[2\tilde{\mu}\,(\overleftrightarrow{\tilde{\nabla}\tilde{U}})_0\right] \tag{44}$$

$$\frac{\partial\tilde{e}}{\partial\tilde{t}} + \nabla\cdot\vec{\tilde{H}} = R_e^{-1}\tilde{\nabla}\cdot\left[2\tilde{\mu}\,\vec{\tilde{U}}\cdot(\overleftrightarrow{\tilde{\nabla}\tilde{U}})_0\right] + \left[(\gamma-1)M^2R_eP_R\right]^{-1}\tilde{\nabla}\cdot(\tilde{\lambda}\tilde{\nabla}\tilde{T}) -$$

$$- SR_m^{-1}\tilde{\nabla}\cdot(\tilde{\eta}\tilde{\nabla}\cdot\overleftrightarrow{\tilde{T}}) - 2S\tilde{\nabla}\cdot(\tilde{\eta}\vec{\tilde{J}}_K\times\vec{\tilde{B}}) \tag{45}$$

$$\frac{\partial\vec{\tilde{B}}}{\partial\tilde{t}} - \tilde{\nabla}\times(\vec{\tilde{U}}\times\vec{\tilde{B}}) = -R_m^{-1}\left\{\tilde{\nabla}\times(\tilde{\eta}\tilde{\nabla}\times\vec{\tilde{B}}) - \tilde{\nabla}\times(\tilde{\eta}\vec{\tilde{J}}_K)\right\} \tag{46}$$

$$\vec{\tilde{B}} = \tilde{\nabla}\times\vec{\tilde{A}}$$

$$\vec{\tilde{E}} = -\tilde{\nabla}\tilde{\Phi} - \frac{\partial\vec{\tilde{A}}}{\partial\tilde{t}}$$

In the form in which the Maxwell stress tensor is decomposed the left hand sides of the momentum and energy equations take the forms

$$\frac{\partial\vec{\tilde{M}}}{\partial\tilde{t}} + \tilde{\nabla}\cdot\overleftrightarrow{\tilde{G}} - S\tilde{\nabla}\cdot\overleftrightarrow{\tilde{T}}_* = \frac{\partial\vec{\tilde{M}}}{\partial\tilde{t}} + \tilde{\nabla}\cdot\overleftrightarrow{\tilde{\Gamma}}$$

$$\frac{\partial\tilde{e}}{\partial\tilde{t}} + \tilde{\nabla}\cdot\vec{\tilde{H}} - S\tilde{\nabla}\cdot(\vec{\tilde{U}}\cdot\overleftrightarrow{\tilde{T}}_*) = \frac{\partial\tilde{e}}{\partial\tilde{t}} + \nabla\cdot\vec{\tilde{H}}$$

The nondimensional variables are defined as

$$\tilde{t} = U_0t/L \qquad \tilde{\nabla} = L\nabla$$

$$\vec{\tilde{U}} = \vec{U}/U_0$$

$$\tilde{\rho} = \rho/\rho_0$$

$$\vec{\tilde{M}} = \vec{M}/\rho_0U_0$$

$$\tilde{T} = T/T_0$$

$$\tilde{e} = \tilde{\rho}\left\{\tilde{\epsilon}\left[\gamma(\frac{\gamma-1}{2})M^2\right]^{-1} + \tilde{U}^2\right\} + S\,\tilde{e}_m$$

$$\tilde{\epsilon} = \epsilon/[(\gamma-1)^{-1}RT]$$

$$\tilde{e}_m = (B^2/2\hat{\mu}_0)/(B_0^2/2\hat{\mu}_0)$$

$$\vec{\tilde{E}} = \vec{E}/U_0B_0$$

$$\vec{\tilde{B}} = \vec{B}/B_0$$

$$\vec{\tilde{A}} = \vec{A}/(B_0/L)$$

$$\tilde{\Phi} = \Phi/(U_0B_0L)$$

$$\vec{\tilde{J}} = \vec{J}/(\hat{\mu}_0^{-1}B_0/L)$$

$$\vec{\tilde{J}}_K = \vec{J}_K/(\sigma_0U_0B_0)$$

$$\overleftrightarrow{\tilde{G}} = \tilde{\rho}\vec{\tilde{U}}\,\vec{\tilde{U}} + \left[(\gamma M^2)^{-1}\tilde{p} + S\tilde{p}_m\right]\overleftrightarrow{I}$$

$$\tilde{\Gamma} \equiv \tilde{\rho}\,\vec{\tilde{U}}\,\vec{\tilde{U}} + (\gamma M^2)^{-1}\,\tilde{p}\overleftrightarrow{I} - S\,\overleftrightarrow{\tilde{\mathcal{T}}}$$

$$\tilde{p}_m = p_m/(B_0^2/2\hat{\mu}_0)$$

$$\vec{\tilde{H}} = \left[\tilde{e} + (\gamma M^2)^{-1}\tilde{p} + S\tilde{p}_m\right]\vec{\tilde{U}}$$

$$\vec{\tilde{\mathcal{H}}} \equiv \left[\left(\tilde{e} + (\gamma M^2)^{-1}\tilde{p}\right)\overleftrightarrow{I} - S\,\overleftrightarrow{\tilde{\mathcal{T}}}\right]\cdot\vec{\tilde{U}}$$

$$\overleftrightarrow{\tilde{\mathcal{T}}} = \overleftrightarrow{\mathcal{T}}/(B_0^2/2\hat{\mu}_0)$$

$$\tilde{\lambda} = \lambda/\lambda_0 \qquad \tilde{\mu} = \mu/\mu_0 \qquad \tilde{\eta} = \eta/\eta_0$$

where

$$\lambda_0 = \lambda(p_0, T_0), \qquad \mu_0 = \mu(p_0, T_0), \qquad \eta_0 = \eta(p_0, T_0).$$

The state equations (38), (30) in nondimensional form are

$$\tilde{p} = \gamma(\gamma-1)M^2\left[\tilde{e} - S\tilde{e}_m - \tilde{M}^2/\tilde{\rho}\right]$$

$$\tilde{T} = \frac{\tilde{p}}{\tilde{\rho}}$$

It can be seen that the general viscous hydromagnetic equations contain six fundamental nondimensional parameters. These are

M	Mach number	$U_0/(\gamma p_0/\rho_0)^{1/2}$
S	Interaction parameter	$(B_0^2/2\hat{\mu}_0)/(\rho_0 U_0^2)$
R_m	Magnetic Reynolds number	$(U_0 L/\eta_0)$
R_e	Viscous Reynolds number	$\rho_0 U_0 L/\mu_0$
P_R	Viscous Prandtl number	$(C_p \mu_0/\lambda_0)$

We note that the Alfvén speed C_A is defined as

$$C_A = \left(B^2/\hat{\mu}_0\rho\right)^{1/2}$$

and the Alfvén Mach number is $M_A = U/C_A$. Hence the interaction parameter S is also twice the reciprocal of the square of the Alfvén Mach number.

For flows in the absence of viscous and diffusion effects $R_m \to \infty$, $R_e \to \infty$ we obtain the inviscid hydromagnetic equations:

$$\frac{\partial\tilde{\rho}}{\partial\tilde{t}} + \tilde{\nabla}\cdot\vec{\tilde{M}} = 0 \qquad (47)$$

$$\frac{\partial\vec{\tilde{M}}}{\partial\tilde{t}} + \nabla\cdot\left[\vec{\tilde{G}} - S\,\vec{\tilde{T}}_*\right] = 0 \qquad (48)$$

$$\frac{\partial \tilde{e}}{\partial \tilde{t}} + \nabla \cdot \left[\vec{\tilde{H}} - \vec{\tilde{U}} \cdot \vec{\tilde{T}}_* \right] = 0 \tag{49}$$

$$\frac{\partial \vec{\tilde{B}}}{\partial \tilde{t}} - \tilde{\nabla} \times (\vec{\tilde{U}} \times \vec{\tilde{B}}) = 0 \tag{50}$$

The jump equations across hydromagnetic shocks immediately follow from Eqs. (47)-(50).

$$\left\{ \vec{\tilde{M}} \right\} = 0 \tag{51}$$

$$\left\{ \vec{\tilde{G}} - S\, \vec{\tilde{T}}_* \right\} = 0 \tag{52}$$

$$\left\{ \vec{\tilde{H}} - \vec{\tilde{U}} \cdot \vec{\tilde{T}}_* \right\} = 0 \tag{53}$$

$$\left\{ \vec{n} \times (\vec{\tilde{U}} \times \vec{\tilde{B}}) \right\} = 0 \tag{54}$$

where $\{\ \}$ denotes the difference in the quantity across the shock surface and $\vec{n}$ is the normal to the shock surface.

Since the electrical conductivity achievable in nonideal plasma is large but finite, the magnetic Reynolds numbers are not infinite but perhaps vary in the range $1 \leq R_m \leq 20$.

In this range, the appropriate system is the inviscid, finite conductivity hydromagnetic system:

$$\frac{\partial \tilde{\rho}}{\partial \tilde{t}} + \tilde{\nabla} \cdot \vec{\tilde{M}} = 0 \tag{55}$$

$$\frac{\partial \vec{\tilde{M}}}{\partial \tilde{t}} + \tilde{\nabla} \cdot \vec{\tilde{\Gamma}} = 0 \tag{56}$$

$$\frac{\partial \tilde{e}}{\partial \tilde{t}} + \tilde{\nabla} \cdot \vec{\tilde{H}} = -SR_m^{-1} \tilde{\nabla} \cdot (\tilde{\eta} \tilde{\nabla} \cdot \overleftrightarrow{\tilde{T}}) \tag{57}$$

$$\frac{\partial \vec{\tilde{B}}}{\partial \tilde{t}} - \tilde{\nabla} \times (\vec{\tilde{U}} \times \vec{\tilde{B}}) = -R_m^{-1} \tilde{\nabla} \times (\tilde{\eta} \tilde{\nabla} \times \vec{\tilde{B}}) \tag{58}$$

or in the alternative form, the momentum and energy equations are

$$\frac{\partial \vec{\tilde{M}}}{\partial \tilde{t}} + \tilde{\nabla} \cdot \overleftrightarrow{\tilde{G}} = S \tilde{\nabla} \cdot \overleftrightarrow{\tilde{T}}_* \tag{56a}$$

$$\frac{\partial \tilde{e}}{\partial \tilde{t}} + \tilde{\nabla} \cdot \vec{\tilde{H}} = S \tilde{\nabla} \cdot (\vec{\tilde{U}} \cdot \overleftrightarrow{\tilde{T}}_*) - SR_m^{-1} \tilde{\nabla} \cdot (\tilde{\eta} \tilde{\nabla} \cdot \overleftrightarrow{\tilde{T}}) \tag{56b}$$

2.6 Applied and Induced Fields

Let us separate the magnetic field $\vec{B}$ into an applied portion $\vec{B}^{(0)}$ sustained by currents external to the plasma and plasma induced portion $\vec{B}^{(i)}$ which results from currents flowing within the plasma:

$$\vec{B} = \vec{B}^{(0)} + \vec{B}^{(i)} \tag{57}$$

The induction equation, Eq. (58), then becomes

$$\begin{aligned} \frac{\partial \vec{\tilde{B}}^{(i)}}{\partial \tilde{t}} - \tilde{\nabla} \times (\vec{\tilde{U}} \times \vec{\tilde{B}}^{(i)}) &= -R_m^{-1} \left\{ \tilde{\nabla} \times (\tilde{\eta} \tilde{\nabla} \times \vec{\tilde{B}}^{(i)}) - \tilde{\nabla} \times (\tilde{\eta} \vec{\tilde{J}}_K) \right\} \\ &\quad - R_m^{-1} \tilde{\nabla} \times (\tilde{\eta} \nabla \times \vec{\tilde{B}}^{(0)}) - \dot{\vec{\tilde{B}}}^{(0)} \end{aligned} \tag{58}$$

where $\frac{\partial \vec{\tilde{B}}^{(0)}}{\partial \tilde{t}}$ is denoted $\dot{\vec{\tilde{B}}}^{(0)}$

3.0 QUASI-ONE-DIMENSIONAL TRANSIENT MAGNETOGASDYNAMICS OF HYPERVELOCITY PULSED FLOWS

3.1 Plasma Flow Configuration

We now consider the behavior of shock generated magnetohydrodynamic interaction and low to high magnetic Reynolds numbers according to a quasi-one-dimensional description. Such a flow consists of a hot plasma "plasmoid" formed between a driven ionizing shock wave and its following contact surface. The plasmoid is created by a sudden release of energy in a driver section which is in contact with a test gas in which the plasmoid propagates. Such a flow may be driven, for example, by the use of focused chemical explosives. [1], [2]

The conducting plasmoid enters a region in which an externally imposed magnetic field $\vec{B}_0$ and electrodes coupled to an external circuit exist (Fig. 3-1). The plasma conducts current to this external circuit and is subject to *Lorentz forces and Joule heating as it propagates through* the magnetic field. If the explosion drive is a chemical source, such a plasmoid will be of the order of 5-20 cm in length in traversing a magnetic field region of the order of 100 cm at velocities of the order of 10^4 m s^{-1}. The plasmoid may exist at pressures up to 1 k bar and energies of 5 eV.

If σ_0, ρ_0, U_0 are the characteristic electrical conductivity, mass density and velocity within the plasmoid, the flow may be specified by an interaction number i and magnetic Reynolds number r_m (in addition to the gasdynamic Mach number).

$$i = \frac{\sigma_0 B_0^2}{\rho_0 U_0} \qquad\qquad r_m = \hat{\mu}_0 \sigma_0 U_0$$

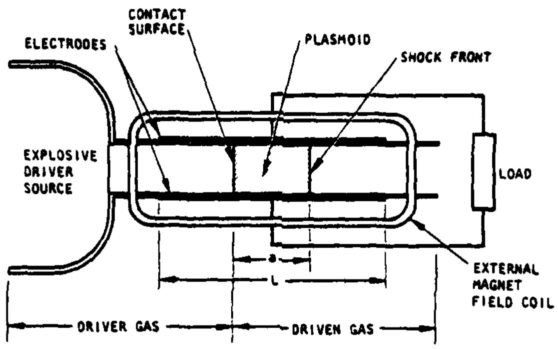

STD 9-2974

Fig.3-1. Schematic of explosion driven plasmoid flow.

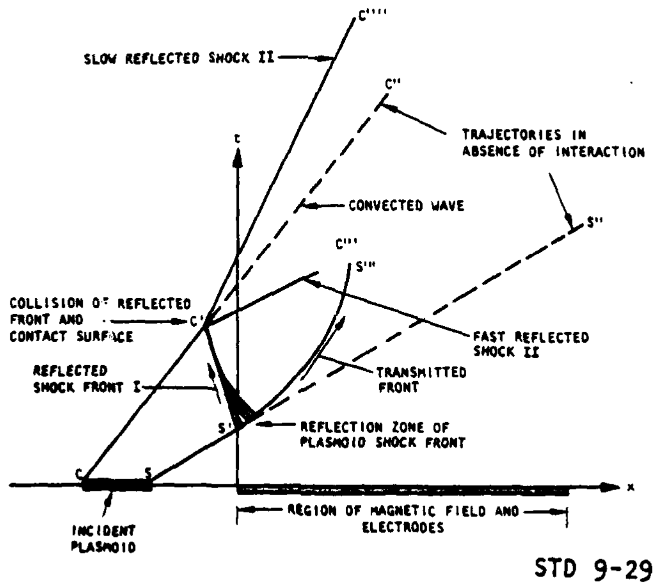

STD 9-2975

Fig.3-2. Space-time diagram of strong interaction hypervelocity plasmoids. Plasmoid trajectory in the limit of vanishing interaction is delimited by the shock front trajectory S S' S'' and contact surface trajectory C C' C''. Plasmoid shock front reflection S'C' and transmission S'S'' are initiated at encounter with magnetic field. Contact surface encounters reflected front at C' which generates fast reflected shock II (C'C'''), slow reflected shock II (C'C''''), and convected wave (C'C'').

For an interaction region of length L, the nondimensional numbers are defined as

$$I \equiv \int_0^L i\,dx \qquad\qquad R_m \equiv \int_0^L r_m\,dx \tag{59}$$

When $R_m >> 1$, the appropriate measure of the interaction is the parameter S' defined as

$$S' \equiv \left(B_0^2/\hat{\mu}_0\right) / \langle \rho U^2 \rangle \tag{60}$$

where the spatial average $\langle\,\rangle$ is over the electrically conducting portion of the region L. For a uniform plasmoid of length a, these numbers become $I = \sigma_0 B_0^2\, a/\rho_0 U_0$, $R_m = \sigma_0 \mu_0 U_0 a$, $S' = I/R_m$.

Pulsed magnetohydrodynamic flows have been examined in the case of low magnetic Reynolds number ($R_m << 1$) and weak interaction ($I \lesssim 1$) [3],[4]. Because of the low interaction, these studies revealed simple current flow through the plasmoid and weak magnetohydrodynamic deceleration.

The transverse ionizing shock-wave which forms the front of the plasmoid has been extensively studied in the limit of infinitely large magnetic Reynolds number [5],[6]. In addition to the exposition of the general Rankine-Hugoniot conditions for these shocks [5] it has also been demonstrated that such shock waves can be reflected as well as transmitted upon encounter with an externally imposed magnetic field. These studies also showed that the electric field in front of the shock must be self-consistently determined with the dynamical state behind the shock and the electrical boundary conditions imposed upon the gas [6].

In the present study, we examine the magnetohydrodynamics of the whole plasmoid in its encounter with, and transit through an externally imposed magnetic field. We show that under conditions of strong interaction, hypervelocity plasmoids can possess a rich variety of magnetohydrodynamic phenomena including magnetically reflected shock waves, embedded MHD discontinuities, and significant periods of transonic flow within the plasmoid. In particular, we reveal the dynamics of reflected and transmitted waves through the plasmoid in both the low and high magnetic Reynolds number regime. We reveal the behavior of electrothermally unstable plasmoids. We show that, in general, the plasmoid is not delimited by the region between the shock front and contact surface. Instead, the plasmoid develops its own internal, evolving structure governed by the mutual interaction of self-heating and self-induced fields.

Shock-generated hypervelocity flows of this kind are subject to a variety of nonideal phenomena. These include wall interaction effects (viscous losses, gas leakage, and ohmic voltage drops in boundary layers), thermal radiation losses, and kinetic/ionization relaxation effects behind shock waves. In the present study we ignore these effects and examine those phenomena which arise specifically from the magnetohydrodynamic interaction.

In Part 3.2 we present the quasi-one-dimensional version of the system of equations discussed in Part 2. In Part 3.3 we examine the dynamics of strong interaction plasmoids with an applied magnetic field but at low magnetic Reynolds number. In Part 3.4 we similarly consider strong interaction plasmoids but at large magnetic Reynolds number. In Part 3.5 we illustrate the behavior of "transitional" plasmoids.

These are flows in which the plasmoid enters the magnetic field at relatively low values of interaction parameter and magnetic Reynolds number. As a result of self Joule heating, however, the plasmoid conductance is elevated as it progresses through the field carrying it into the strong interaction, high magnetic Reynolds number regime.

3.2 The One-Dimensional Description

We consider a quasi-one-dimensional description of the gas moving over the spatial coordinate x in time t. If the equations of Section 2 are averaged over the cross section of the duct, we obtain the quasi-one-dimensional forms

$$\frac{\partial \underline{W}}{\partial t} = - \frac{\partial \underline{F}}{\partial x} + \Xi \tag{61}$$

where $\underline{W}(x,t)$ is the vector of mass, momentum, and total energy densities

$$\underline{W}(x,t) = \begin{bmatrix} \rho \\ m \\ e \end{bmatrix} \tag{62}$$

In the above, the following definitions apply

$$m = \rho U$$

$$e = \rho(\mathcal{E} + U^2/2$$

where all quantities are to be interpreted as averages over the duct cross section. The magnetic field $\vec{B}_i$ is that induced by the plasma currents where $\vec{B}_0$ is the applied field:

$$\vec{B} = \vec{B}_0 + \vec{B}_i$$

The convected fluxes of mass, momentum, and energy are contained in the vector $\underline{F}$ while Ξ contains the Lorentz force and power associated with the magnetic field and the Joule dissipation. These are expressed in terms of current density $\vec{J}$ and magnetic field $\vec{B}$:

$$\underline{F} = \begin{bmatrix} m \\ m^2/\rho + p + B_i^2/2\hat{\mu}_0 \\ m/\rho\,(e+p) \end{bmatrix} \qquad \underline{\Xi} = \begin{bmatrix} 0 \\ (\vec{J}\times\vec{B}_0)_x \\ J^2/\sigma - \vec{J}\cdot(\vec{U}\times\vec{B}) \end{bmatrix} \tag{63}$$

In this illustration study we assume that the kinetic effects are confined to the relaxation layer at the shock, and further, that the relaxation layer is thin compared to the overall thickness of the plasmoid.

For the simple geometry (x,y,z) of Fig.3-1, the magnetic field $\vec{B}$ is given by $\vec{B}(0,0,B)$, the electric field by $\vec{E} = \vec{E}(0,E,0)$, and the current by $\vec{J} = \vec{J}(0,J,0)$. The description for the near fields J, B_i of the plasmoid is then given by Ohm's law and the Maxwell equation in the MHD approximation:

$$J = \sigma\left(E - UB_i - UB_0\right) \tag{64}$$

$$\frac{\partial B_i}{\partial x} = -\eta\,(E - UB_i - UB_0) \tag{65}$$

where $\eta \equiv (\hat{\mu}_0\sigma)^{-1}$ is the magnetic diffusivity.

External interaction conditions with an external circuit including inductive coupling with the applied magnetic field coil are required to

complete the description of actual flow situations. Rather than include such circuit detail in these illustrations we assume that the external circuit is configured so that an electric field $\vec{E} = \vec{E}(0, E, 0)$ is maintained within the interelectrode region whose magnitude is uniform in space and given by

$$E = \kappa \langle UB \rangle$$

where κ is a "load" parameter $(0 \leq \kappa \leq 1)$. For a passive external circuit, the value $\kappa = 0$ corresponds to a shorted external circuit; for $\kappa = 1$ the external circuit is open circuited.

The fluid variables ρ, p, T, σ, U are nondimensionalized by the values $\rho_0, p_0, T_0, \sigma_0, U_0$ characterizing the interior of the initial plasmoid before encounter with the magnetic field. Nondimensional space and time $\bar{x}, \bar{t}$ are defined in terms of x, nondimensionalized by the plasmoid length a, and t by a/U_0. The nondimensional parameters governing the interaction are the Mach number M, the gas heat ratio γ, either of the interaction parameters I or S', and the magnetic Reynolds number R_m.

Boundary and Initial Conditions

In the limit of $R_m \to \infty$, the system consisting of Eqs. 59 , and (62) is fully hyperbolic. For finite R_m, the system is mixed hyperbolic/ parabolic with embedded regions where resistive effects occur. The boundary and initial conditions which specify the interaction problem for an explosion generated plasmoid encounter with a magnetic field are as follows. As an initial condition we take an idealized explosion driven

flow in which the plasmoid of given breadth a occupies the hot zone between contact surface and shock front [9] (Fig. 3-3). At time $t = 0$ the shock front is located at the edge of the magnetic field. Over the time scale for the dynamics of interest the shock front of the plasmoid will run continuously into the quiescent driver gas while the backward running rarefaction continuously runs into the explosive source. Hence the boundary conditions for the fluid equations are those of specified explosion and quiescent states at the boundaries $x = +L_1$, $x = -L_2$ respectively.

The boundary condition for the induced magnetic field B_i from Eq. (61) is that of symmetry across the overall plasmoid so that at $x = L_1$, $x = -L_2$ which lie outside the region of any current flow

$$B_i(-L_2, t) = -B_i(L_1 t)$$

The applied magnetic field B_0 is uniform in both space and time.

Numerical Procedures

The solutions to the initial-value problems formulated above and to be discussed in Section 3.3, 3.4, and 3.5 are computationally generated with second order accurate explicit finite difference operators. The hyperbolic system is treated with the MacCormack version of the Lax-Wendroff-Richtmyer operator [10]. For the space-time grid utilized, comparisons were made with the analytically available solutions for the zero and infinite R_m, zero interaction limits. At the extreme pressure ratios of 10^5 between driver and driven gas for these explosion generated plasmoids, the maximum variations between the computationally generated and analytical solutions within the plasmoid (expressed as a fraction of the analytical solution) are 0.025 in velocity, 0.04 in pressure, and 0.08 in temperature.

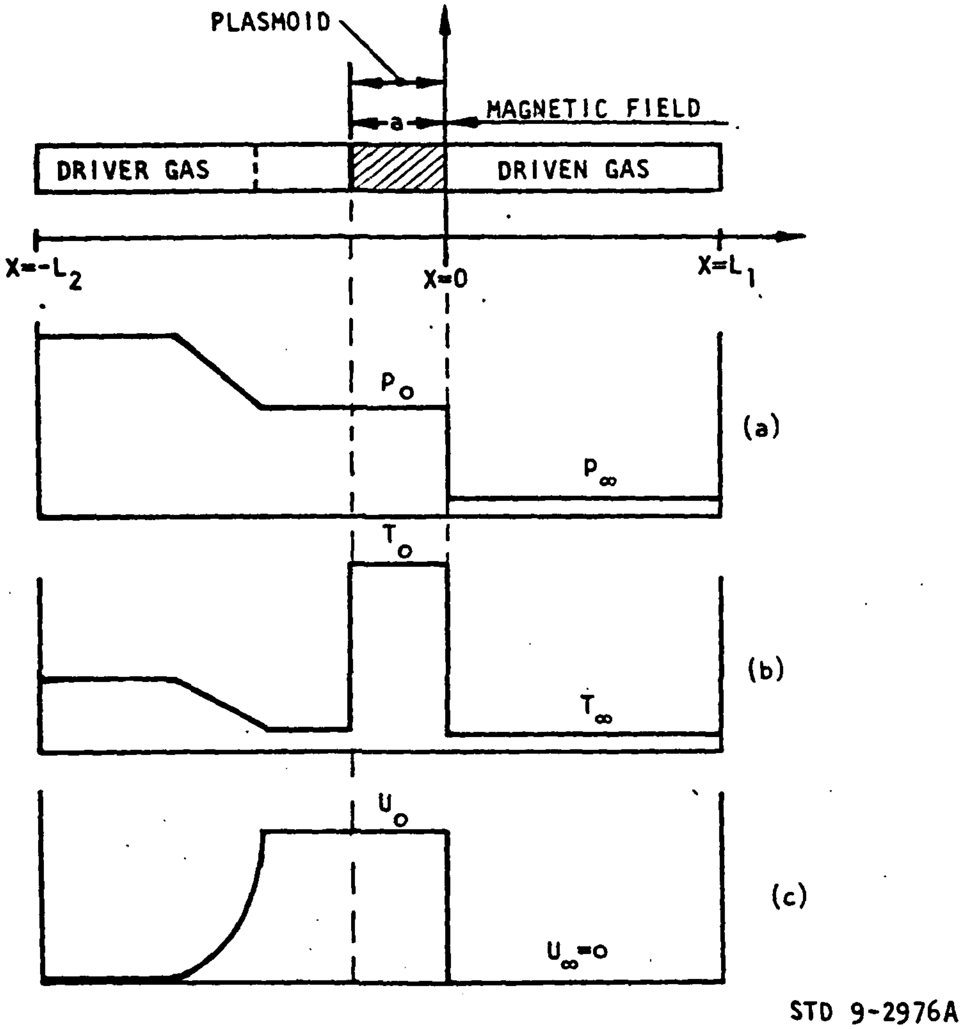

Fig. 3-3. Initial condition for plasmoid interaction for the pressure (a), temperature (b), and velocity (c). Shock front of plasmoid of given breadth a located at magnetic field edge at time t = 0

STD RESEARCH CORPORATION

3.3 Interaction at Low Magnetic Reynolds Number

We now proceed to the first of several illustrations of the foregoing description. We consider first the strong interaction of a plasmoid with the magnetic field but at low magnetic Reynolds number. In Fig. 3-2 the kinematics of this situation are shown. When the incident plasmoid encounters the magnetic field, the leading shock front may be both transmitted and reflected. In the case of reflected fronts, the rear (contact surface) of the plasmoid subsequently interacts with the reflected shock front. This colliding disturbance then radiates a fast and slow reflected shock (denoted shock II) back through the plasmoid (which consists of subsonic flow behind the reflected shock front) where it then collides with the now strongly decelerated shock front.

For the illustration shown here, we select a plasmoid with Mach number $M = 1.64$, interaction parameters $I = 20$, $S = 200$, and Reynolds number $R_m = 0.1$, just before encountering the magnetic field. The full conditions for the flow are given in Table I. We impose the condition that the electrical conductivity is spatially uniform within the high temperature plasmoid (we consider electrical conductivity functions which are consistently coupled to the gas thermodynamic state in Part 3.4). This uniform conductivity distribution is achieved in the computations with the model conductivity function

$$\sigma = \begin{cases} 0 & T/T_0 < 1/3 \\ \sigma_0 & T/T_0 \geq 1/3 \end{cases}$$

TABLE I

Conditions for Interaction at Low Magnetic Reynolds Number

T_∞ ≡ Quiescent driven gas temperature

p_∞ ≡ Quiescent driven gas pressure

$M = 1.64$	$\gamma = 1.5$
$p_0/p_\infty = 232$	$I = 20$
	$R_m = 0.1$
$T_0/T_\infty = 45$	$\kappa = 0.5$

STD 9-3050

TABLE II

Conditions for Interaction at High Magnetic Reynolds Number

$M = 1.64$	$\gamma = 1.5$
$p_0/p_\infty = 232$	$I = 20$
	$R_m = 5$
$T_0/T_\infty = 45$	$\kappa = 0.5$

STD 9-3051

TABLE III

Conditions for Transitional Plasmoid

$M = 1.64$	$\sigma_0 = 1080$
$p_0/p_\infty = 232$	$n = 3.11$
$T_0/T_\infty = 45$	$\bar{Z}^2_{eff}/\ln\Lambda = 0.16$
$\gamma = 1.5$	$\kappa = 0.5$

STD 9-3052

which effectively switches on a constant conductivity σ_0 within the plasmoid and switches the conductivity off outside the zone in which the plasmoid exists. The dynamics of the interaction are exhibited in Figs. 3-4 and 3-5. When the plasmoid shock front encounters the magnetic field, it is both reflected and transmitted. The reflected shock I collides with the contact surface and initiates a fast reflected shock II and a slow reflected shock. The fast reflected shock II reestablishes high velocity flow through the plasmoid and reencounters the transmitted shock front which has been decelerated. During this period of strong wave dynamics the current distribution within the plasmoid is strongly affected (Fig. 3-5). The current is diminished to very small values during the period of plasmoid deceleration behind the reflected shock I, and the returns back to enhanced levels after passage of the fast reflected shock II. The low magnetic Reynolds number of the plasmoid allows the current to diffuse nearly uniformly throughout its breadth.

3.4 Interaction at High Magnetic Reynolds Number

We next consider the behavior of a uniform conductivity plasmoid in the high magnetic Reynolds number regime. For this case the incident plasmoid has an interaction parameter I = 20 as in the previous illustration but a magnetic Reynolds number $R_m = 5$. Correspondingly, the interaction number S' has the reduced value S' = 4. The full conditions for this flow are given in Table II. The encounter of this plasmoid with the magnetic field is similar to that of Part III. The features peculiar to the higher Reynolds number are best perceived in the current distribution of Fig. 3-7 which is more nonuniform compared to that of Fig. 3-8. When the current levels rise behind the reflected shock II, they do so by directly following the shock until it merges with the transmitted front. The current

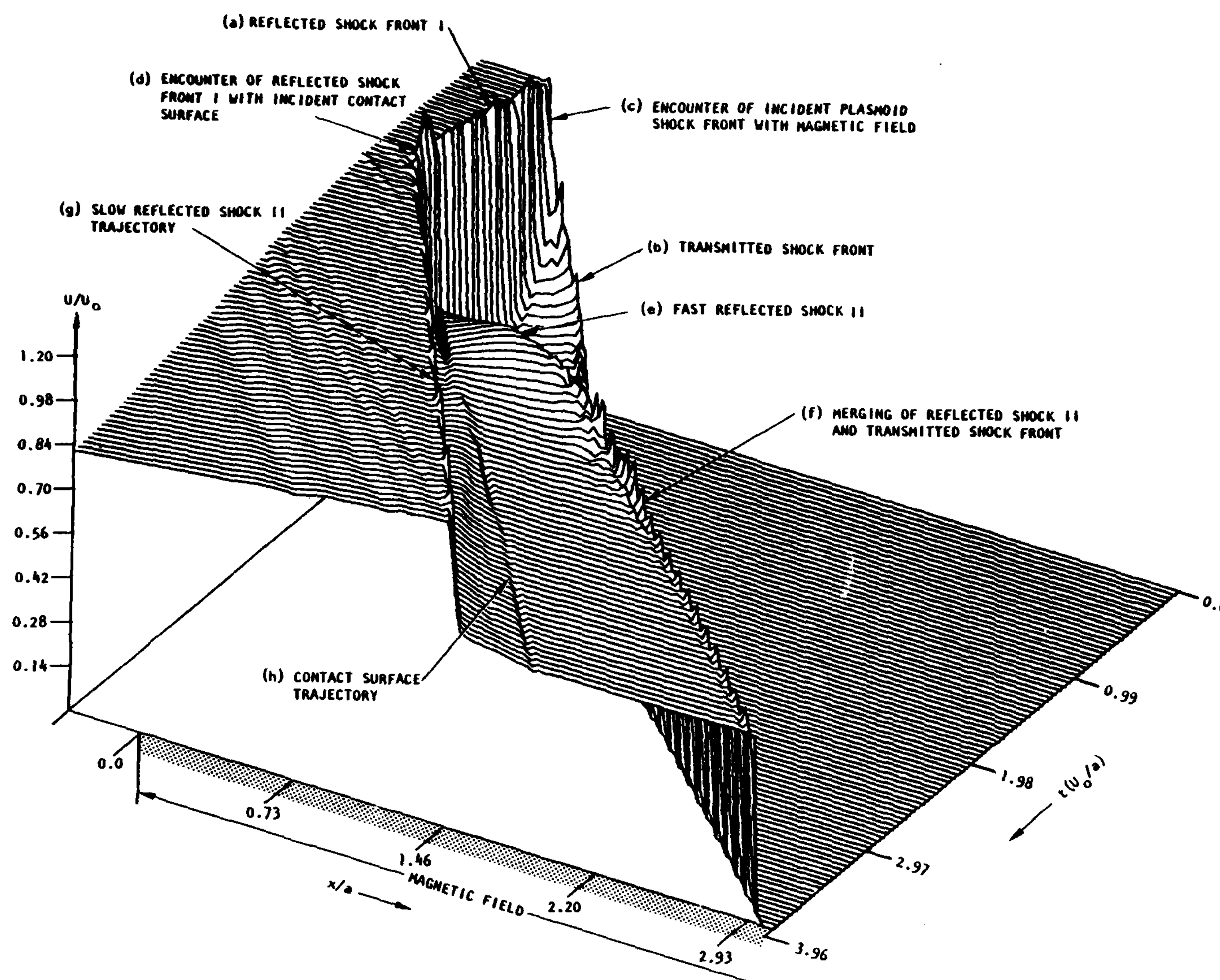

STD 9-2976

Fig.3-4. Velocity field of plasmoid in transit through an applied magnetic field under strong interaction (I = 20), low magnetic Reynolds number ($R_m = 0.1$) conditions. Shock front of plasmoid is both reflected from magnetic field (a) and transmitted into magnetic field (b). Reflected wave I (a) collides with contact surface (d) and initiates a fast reflected shock II (e) and slow reflected shock (g). Reflected wave II (e) merges with transmitted shock front (f). Contact surface (h) separates conducting from nonconducting gas behind. Note transitory region of sharply diminished velocities within the plasmoid during the period of reflection and rereflection of the shock front.

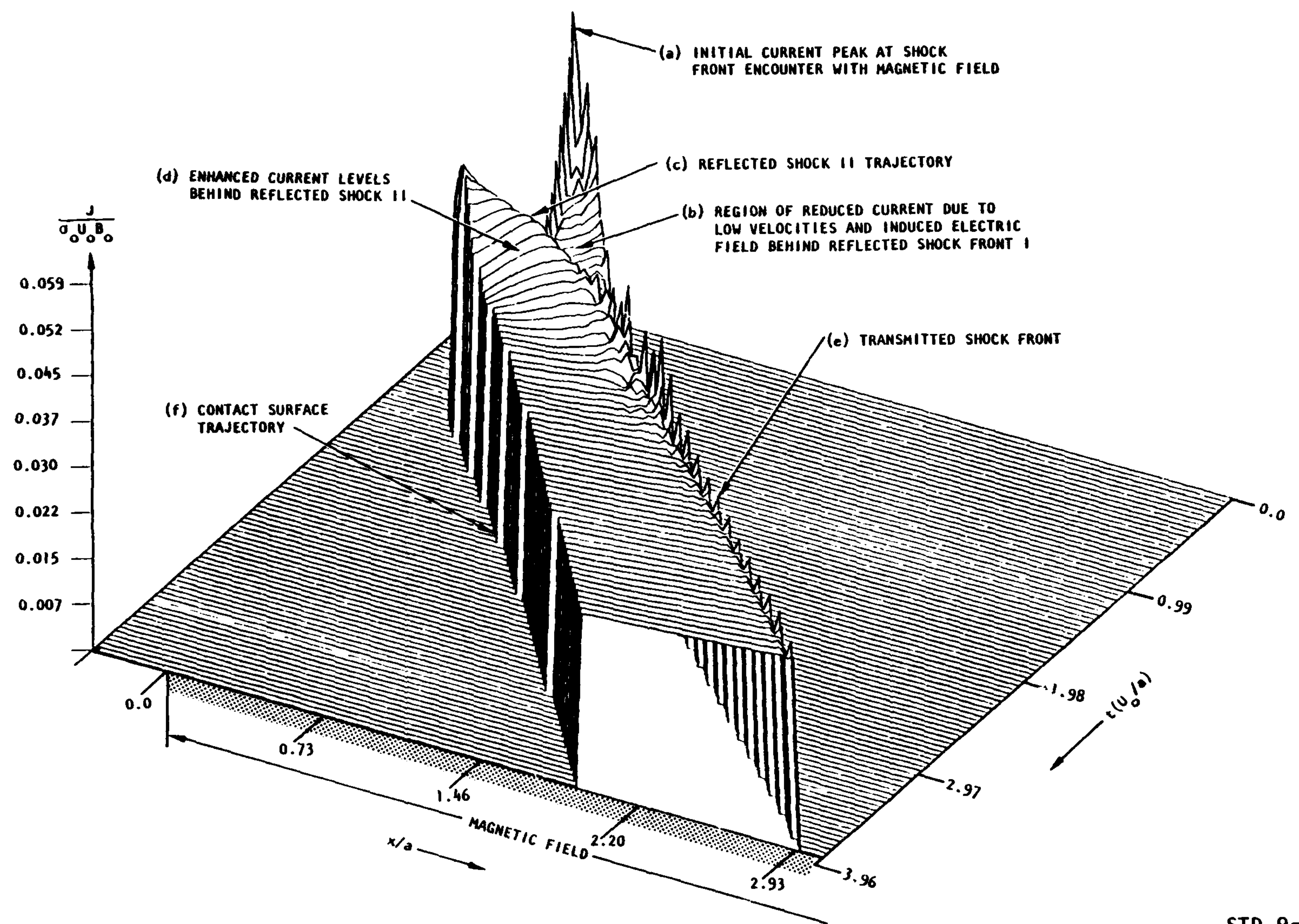

STD 9-2977

Fig.3-5. Current density distribution for conditions of Fig. 3-4. Initial peak of current density (a) diminishes sharply as plasmoid velocities diminish behind reflected shock front I(b). After passage of reflected shock II (c) current levels rise (d) and remain uniform through plasmoid. With uniform conductivity model, conductivity is uniform between shock front (e) and contact surface (f). At low magnetic Reynolds number ($R_m = 0.1$), current is diffused nearly uniformly over plasmoid.

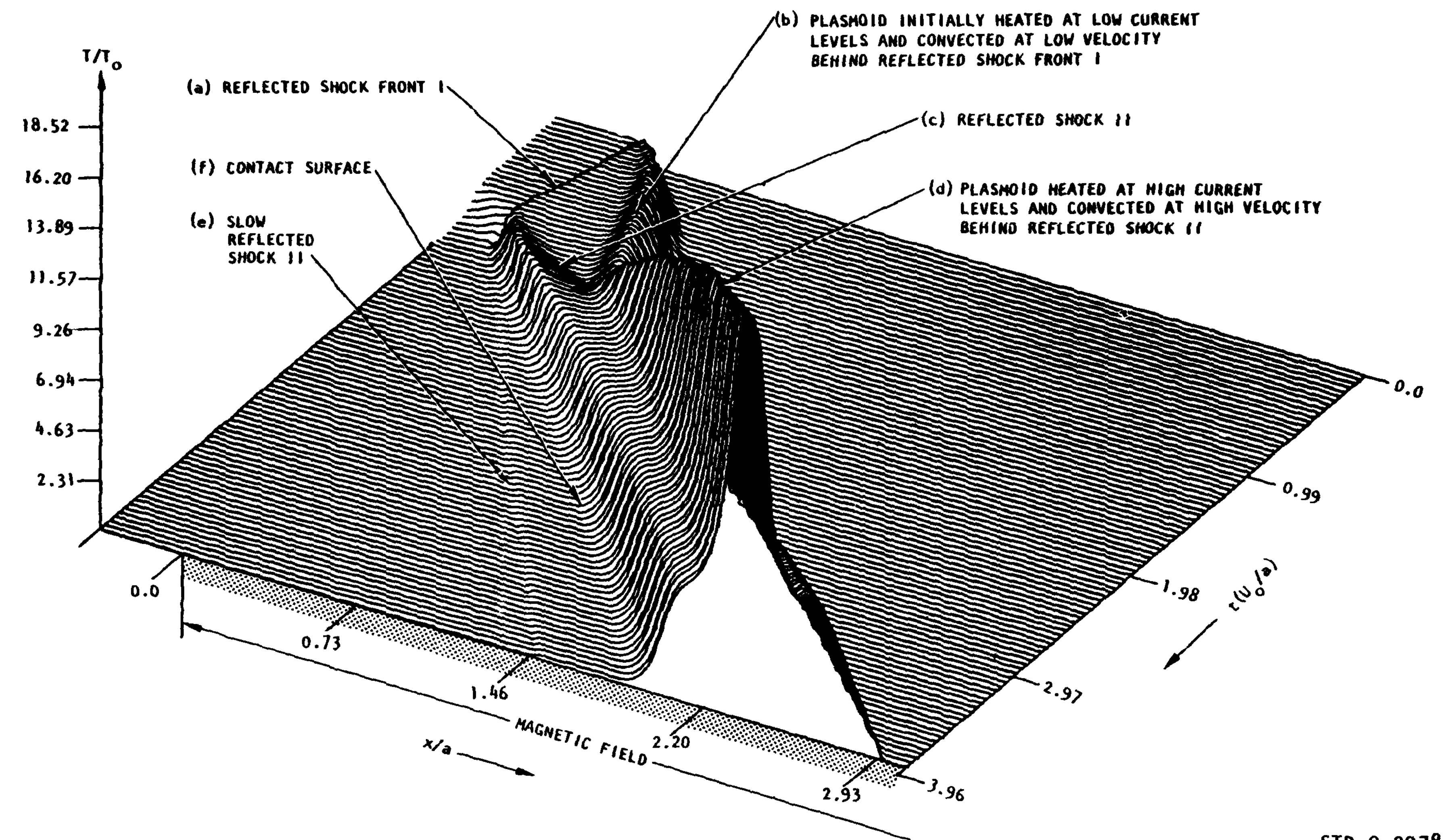

STD 9-2978

Fig.3-6. Temperature distribution for conditions of Fig. 3-4. Otherwise uniform temperature of plasmoid is affected by wave dynamics, and most significantly, by Joule heating. Weak initial current levels due to reflected shock front I (a) as shown in Fig. 3-4 lead to weak elevations in temperature due to Joule heating (b). Note that heated region within plasmoid at that time is convected at low velocity. Transmitted shock front is sharply decelerated. Contact surface is much less decelerated during this period. After passage of reflected shock II (c), Joule heating increases significantly thereby elevating plasmoid interior temperature (b). Following passage of reflected shock II, plasmoid interior is convected at velocities ranging between that of front and that of contact surface. Trace (e) is due to the slow reflected shock wave II.

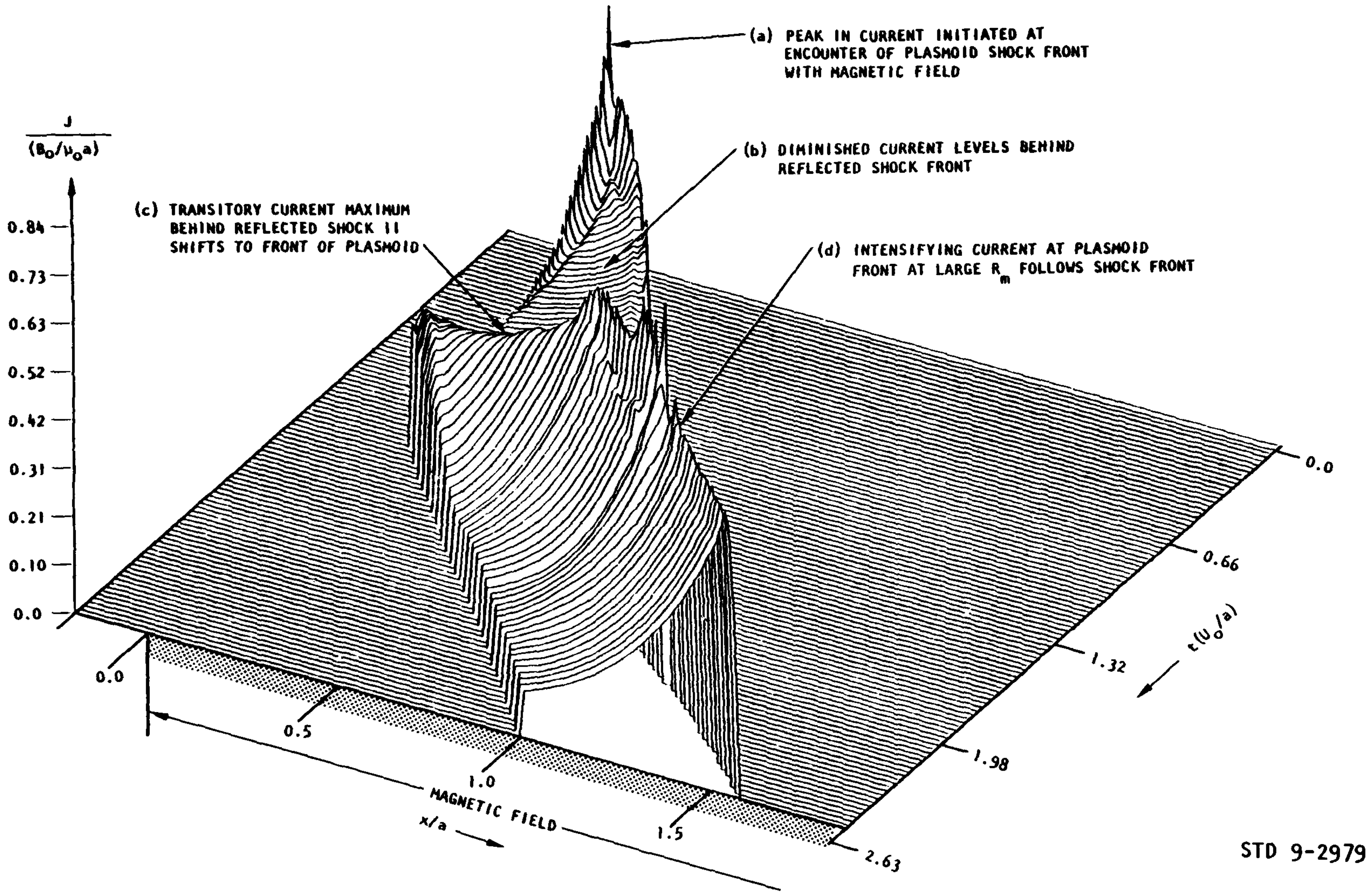

STD 9-2979

Fig. 3-7. Current distribution for a strong interaction plasmoid at $R_m = 5$. Dynamics are similar to those exhibited in Figs. 3-4 thru 3-6, however the larger Reynolds number permits more nonuniform current (and induced magnetic field) distributions. Current pulse initiated by encounter of plasmoid shock front (a) gives way to diminished current levels in low velocity region behind reflected shock front I (b). Current levels rise and shift to front of plasmoid (c), (d) after passage of reflected shock front II. Note that current concentrates immediately behind shock front in contrast to that of Fig. 3-5 (where current is nearly uniform) and that of Fig. 3-10 (where current is nearly absent) behind shock front.

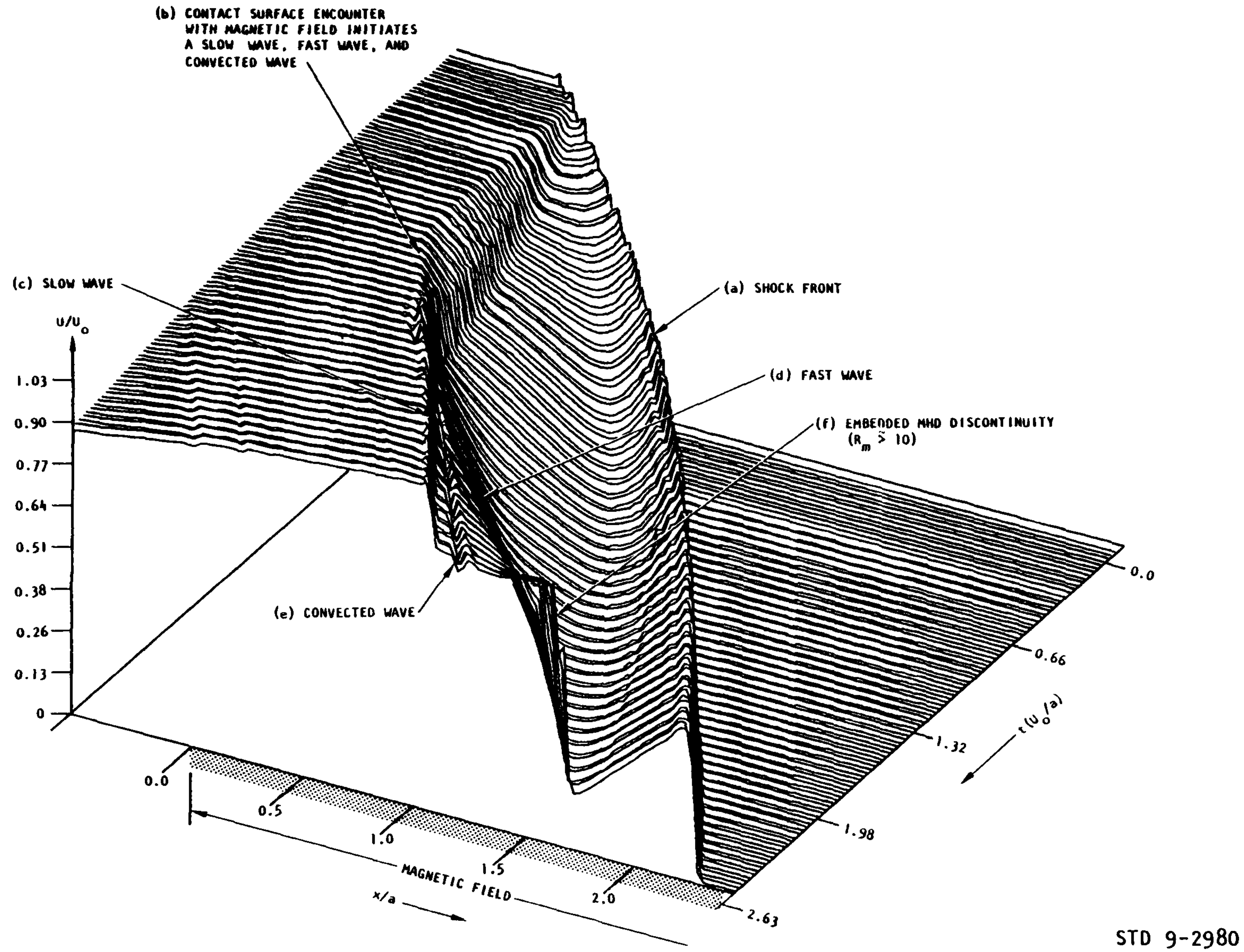

Fig.3-8. Velocity distribution for a transitional plasmoid. Plasmoid enters magnetic field with $I = 1$, $R_m = 1$, $S = 1$. Modest interaction at entry to magnetic field does not generate distinct reflected waves, but rather strong and continuous deceleration. Magnetic Reynolds number and interaction parameters grow during the course of transit. Shock front proceeds through magnetic field with continuous deceleration (a). Once the Reynolds number reaches values $R_m \tilde{>} 10$, the current has become sheet-like with a deflagration-like, intensifying discontinuity within a large subsonic zone of the plasmoid. Contact surface encounter with magnetic field (b) initiates downstream running waves (c), (d), (e).

maximum then remains at the shock front of the plasmoid. As a result of decelerating Lorentz forces concentrated immediately behind the shock front, the shock front is slowed and the overall breadth of the plasmoid is decreased as it progresses through the magnetic field. This is in contrast to the plasmoid dynamics of Parts 3.3 and 3.5.

3.5 Transitional Plasmoids

We now turn to consideration of plasmoid behavior with a coupled electrical conductivity model. In contrast to the previous illustrations in which the conductivity is spatially uniform within the high temperature plasmoid and vanishes outside, we consider a conductivity which is appropriately coupled to the thermodynamic state of the gas. As a result, local regions within the plasmoid can be rendered more conductive by the self Joule heating of the plasmoid. With the electrical conductivity strongly coupled to the Joule dissipation, a plasmoid in the low I, low R_m range can evolve into the large I, large R_m range as it progresses through the magnetic field and experiences further Joule heating. We term such flows "transitional" plasmoids.

We consider a conductivity function of the form

$$\sigma^{-1} = \sigma_{en}^{-1} + \sigma_{ei}^{-1}$$

In the above σ_{en} is an electrical conductivity of a neutral species background and σ_{ei} is the Coulomb conductivity. We use as a summary representation of these two contributions the forms

$$\sigma_{en} = \sigma_0 \left(\frac{T}{T_0} \right)^n$$

$$\sigma_{ei} = 152\ \bar{Z}_{eff}^{-2}\ T^{3/2}/\ell n\Lambda$$

where $\bar{Z}_{eff}$ is the average effective ionic charge and $\sigma_0, T_0, \ell n\Lambda$, $n>0$ are parameters for a given gas.

The conductivity function Eqs. (63)-(64) is dominated by the partially ionized conductivity σ_{en} at low temperature and goes over to the Coulomb (fully-ionized) conductivity at high temperature. This conductivity function has the property $\partial\sigma/\partial T \gtrsim 0$ over the entire range of temperature. Since there are no thermal energy loss mechanisms (which would be principally radiative) included in the model, the plasmoid is unconditionally electrothermally unstable [11], [12]. This convective instability is simply a growth of temperature nonuniformities within the plasmoid due to intensifying Joule heating resulting from growing electrical conductivity.

The interaction of a representative transitional plasmoid is shown in Figs. 3-8 to 3-10. This plasmoid has interaction parameters $I = 1$, $S = 1$ and magnetic Reynolds number $R_m = 1$ just before it enters the magnetic field. The complete conditions for this flow are given in Table III. It should be noted that the interaction at entry into the magnetic field is considerably smaller than the interaction described in Parts 3.3 and 3.4. The plasmoid progresses into the field where it begins to self-heat and decelerate. The modest interaction at plasmoid entry to the magnetic field does not create distinct reflected waves, but rather a strong and continuous deceleration. Magnetic Reynolds number and interaction parameter grow significantly as the plasma is heated. At time $\bar{t} = 2.6$, the magnetic Reynolds number is

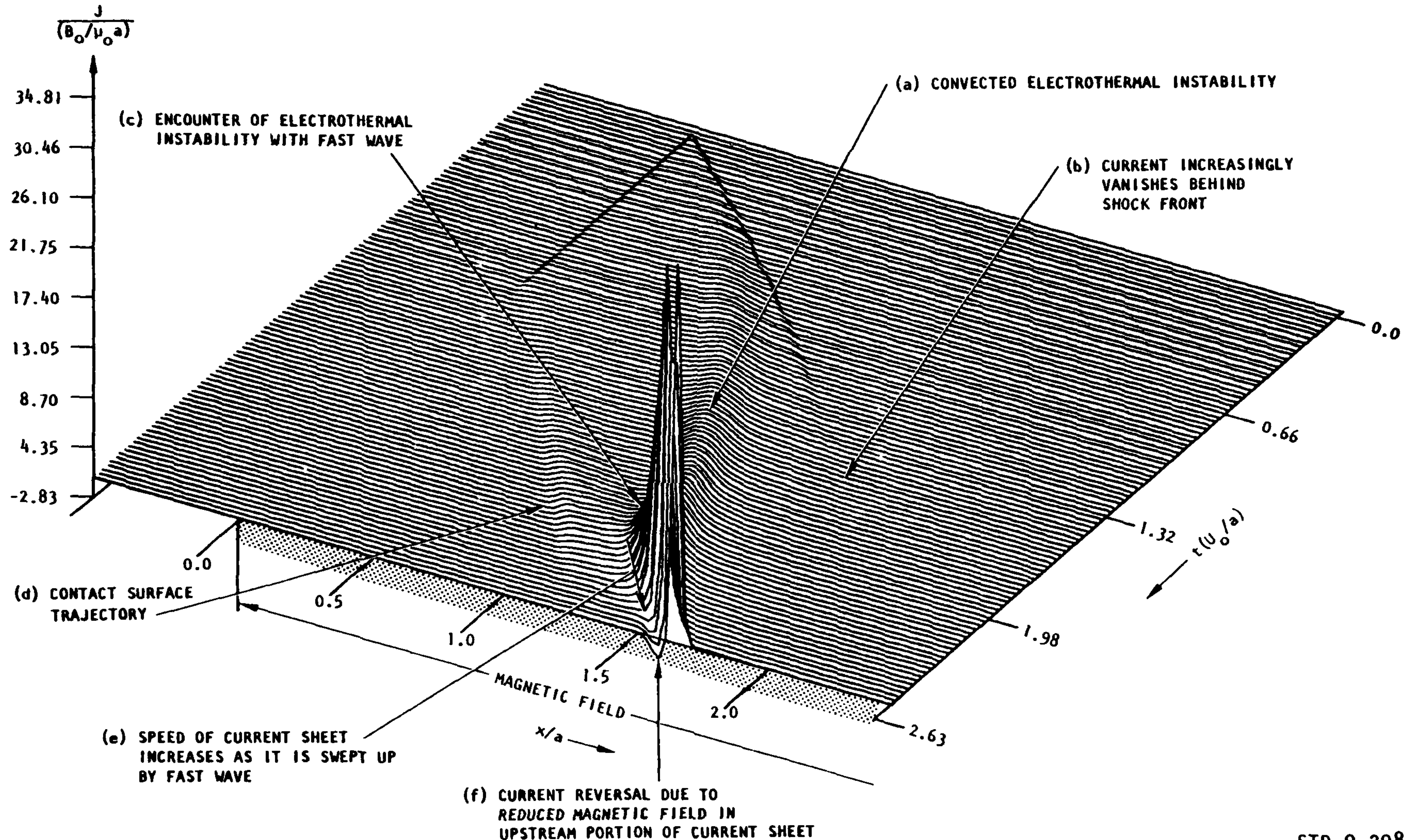

STD 9-2981

Fig. 3-9. Current distribution for transitional plasmoid of Fig. 3-8. Current concentration behind shock front at entry to magnetic field grows (a) with corresponding heating and conductivity enhancement (reflected in temperature field of Fig. 3-10. Shock front propagates ahead (b), but becomes increasingly free of current. Electrothermally heated zone becomes the most highly conducting region of the plasmoid. This heated zone is convected with the gas and strongly decelerated. Sharp rise in temperature and current occurs when unstably evolving current pulse (which is convected) collides with radiated wave (c). Current pulse is then swept up by contact surface and reaccelerated (e). Note current reversal due to sharply reduced magnetic field in upstream portion of current sheet (f).

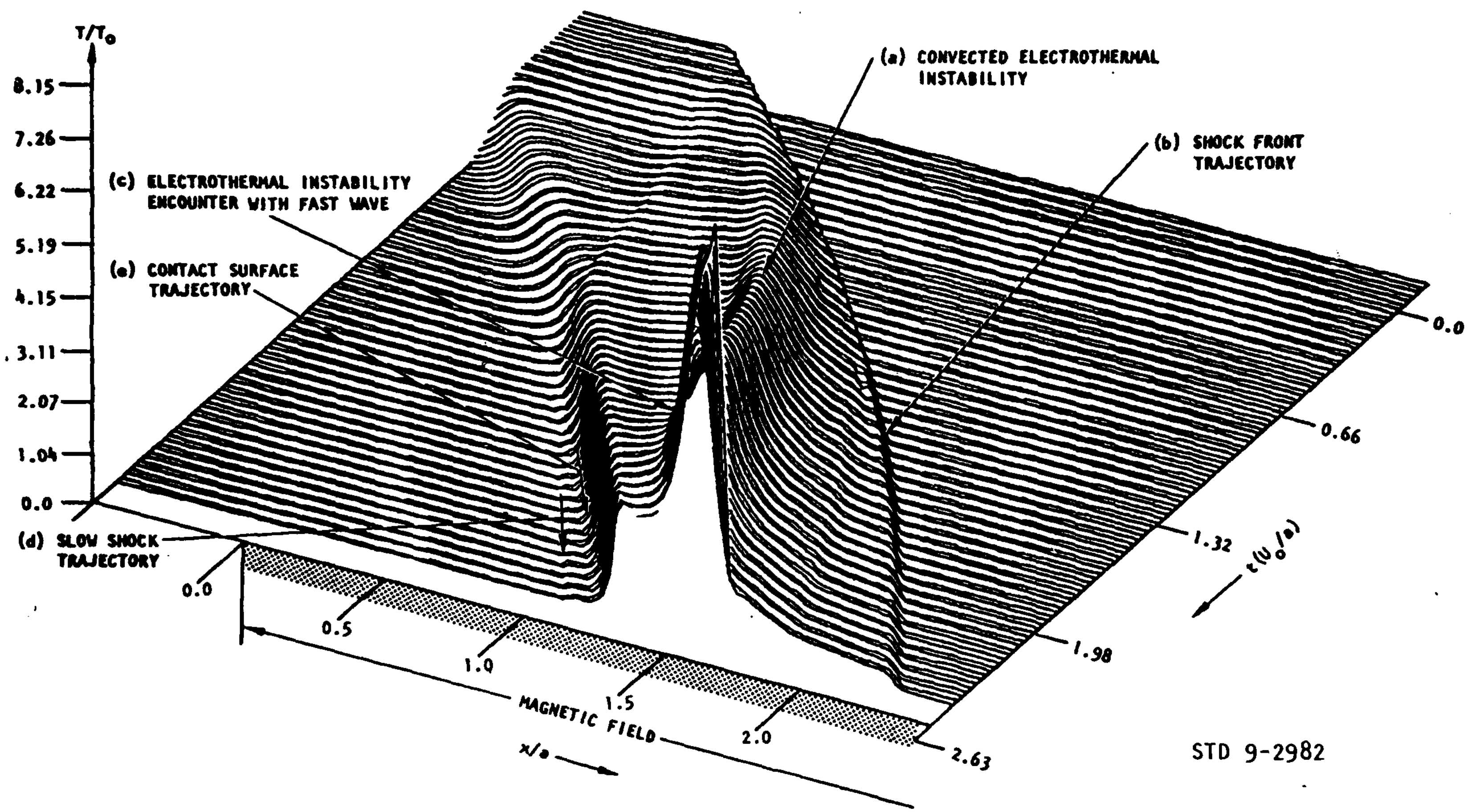

Fig. 3-10. Temperature field corresponding to Figs. 3-8, 3-9 showing developing electrothermal instability.

in excess of 10 and the current has progressively become sheet-like. It should be noted that the current maxima no longer follow immediately behind the transmitted shock front. Rather, the current concentrates in the electrothermally heated zone which is then convected at the local fluid speed rather than radiated at the shock front speed. This decelerating electrothermal instability is then swept up by collision with the waves initiated by the arrival of the contact surface at the magnetic field inlet. A feature of note is the development of reversed current flow in the upstream portion of the current sheet due to the sharply diminished magnetic field behind the current sheet at large R_m.

3.6 Summary Remarks

In this study we have illustrated significant purely magnetogasdynamic phenomena which occur when a hypervelocity pulse of plasma ("plasmoid") encounters an applied magnetic field under strong interaction conditions. With uniform electrical conductivity within the plasmoid (and vanishing electrical conductivity outside), reflection and transmission of the plasmoid shock front are possible coupled with strongly nonuniform current evolution in time. Such plasmoids with large magnetic Reynolds numbers have current distributions (and decelerating Lorentz forces) concentrated immediately behind the shock front. As a result of shock front deceleration, these plasmoids diminish in breadth as they proceed through the magnetic field. With electrical conductivity within the plasmoid coupled to its thermodynamic state, the plasmoid is electrothermally unstable and creates its own, evolving region of enhanced electrical conductance which carries most of the current and is convected at the fluid speed within

the plasmoid. The shock front becomes increasingly free of current and runs progressively farther ahead of the unstable current structure embedded in the plasmoid interior.

Nonideal phenomena such as viscous wall layers, kinetic-relaxation effects behind the shock front, and thermal radiation losses can play important roles in these strong interaction flows. The basic structure of the magnetohydrodynamic interaction itself, however, is a prerequisite to the description and understanding of these additional modifying effects.

4. CURRENT AND MAGNETIC FIELDS IN TWO-DIMENSIONAL HIGH MAGNETIC REYNOLDS NUMBER FLOWS WITH NONUNIFORM VELOCITY AND ELECTRICAL CONDUCTIVITY

4.1 Channel and Applied Magnetic Field Configuration

We now consider some illustrative flows in which the fluid distribution of velocity and electrical conductivity are specified as functions of space and the induced magnetic fields and the plasma currents are to be determined. Three general classes of flow will be examined.

(a) Uniform velocity and conductivity distributions

(b) Nonuniform velocity and conductivity distributions resulting from an hypothesized oblique shock system within the MHD generator duct

(c) Nonuniform velocity and conductivity distributions resulting from supersonic boundary layers on the walls of the MHD generator duct.

All flows exist within the duct geometry and applied magnetic field distribution shown in Figs. 4-1 through 4-10 in which the generator electrode length is equal to the duct height. The magnetic field is given by

$$B^{(0)}(x) = B_m^{(0)} \begin{cases} 0 & |x| \geq \frac{L}{2} \\ \dfrac{1+\exp(-aL)-\exp[-a(x+L/2)]-\exp[a(x-L/2)]}{[1-\exp(-aL/2)]^2} & |x| < \frac{L}{2} \end{cases}$$

where $B_m^{(0)}$ is the maximum applied field. The values selected are $L = 4h$ and $a = 2/h$.

Since these calculations decouple the electricity from the fluid behavior (weak or vanishing interaction) only the magnetic Reynolds number, R_m, is a relevant electrical parameter. All cases include conditions for a magnetic Reynolds number $R_m \geq 1$ which is the range of interest.

4.2 Two-Dimensional Electrical Description

Let us now consider the forms of Eq. (58) appropriate to conduction in the plane perpendicular to an applied magnetic field $\vec{B}^{(0)}$. Let the z axis be aligned with the applied field $\vec{B}^{(0)}$ and let x,y be the coordinates defining the plane of conduction. The current vector then becomes $\vec{\tilde{J}} = \vec{\tilde{J}}(\tilde{J}_x, \tilde{J}_y)$, the magnetic vector becomes $\vec{\tilde{B}} = \vec{\tilde{B}}(0,0,\tilde{B})$, and the velocity $\vec{\tilde{U}} = \vec{\tilde{U}}(\tilde{U}_x, \tilde{U}_y, 0)$, with Eq.(10) taking the form

$$\tilde{J}_x = \frac{\partial \tilde{B}^{(i)}}{\partial \tilde{x}} \qquad J_y = - \frac{\partial \tilde{B}^{(i)}}{\partial \tilde{y}} \tag{66}$$

The induction equation (58) is then

$$\frac{\partial \tilde{B}^{(i)}}{\partial \tilde{t}} + \frac{\partial}{\partial \tilde{x}}(\tilde{U}_x \tilde{B}^{(i)}) + \frac{\partial}{\partial \tilde{y}}(\tilde{U}_y \tilde{B}^{(i)}) = R_m^{-1}\left[\tilde{\eta}\left(\frac{\partial^2 \tilde{B}^i}{\partial \tilde{x}^2} + \frac{\partial^2 \tilde{B}^{(i)}}{\partial \tilde{y}^2}\right) + \right.$$
$$\left. + \frac{\partial \tilde{\eta}}{\partial \tilde{x}}\frac{\partial \tilde{B}^{(i)}}{\partial \tilde{x}} + \frac{\partial \tilde{\eta}}{\partial \tilde{y}}\frac{\partial \tilde{B}^{(i)}}{\partial \tilde{y}}\right] - \frac{\partial}{\partial \tilde{x}}(\tilde{U}_x \tilde{B}^{(0)}) - \frac{\partial}{\partial \tilde{y}}(\tilde{U}_y \tilde{B}^{(0)}) - \dot{\tilde{B}}_0 \tag{67}$$

The boundary conditions appropriate to Eq. (67) are that on insulating boundaries,

$$\tilde{B}^{(i)} = \text{constant} \tag{68}$$

while on conductors

$$\frac{\partial \tilde{B}^{(i)}}{\partial \tilde{n}} = 0 \tag{69}$$

where $\tilde{n}$ is the normal coordinate to the conductor surface.

At steady-state the electric field is derivable from a potential $\tilde{\Phi}$:

$$\vec{\tilde{E}} = -\tilde{\nabla}\tilde{\Phi} \tag{70}$$

Given the induced fields, $\vec{\tilde{B}}^{(i)}$, the potential distribution $\tilde{\Phi}(\vec{\tilde{x}})$ is

$$\tilde{\Phi}(\vec{\tilde{x}}) = \tilde{\Phi}(\vec{\tilde{x}}_0) + \oint_{\vec{\tilde{x}}}^{\vec{\tilde{x}}} \left[-R_m^{-1}(\tilde{\nabla} \times \vec{\tilde{B}}^{(i)}) + \vec{\tilde{U}} \times \vec{\tilde{B}} \right] \cdot d\,\vec{\tilde{s}} \tag{71}$$

where $\oint_{\vec{\tilde{x}}}^{\vec{x}} d\,\vec{\tilde{s}}$ is the line integral along any contour from $\vec{\tilde{x}}_0$ to $\vec{\tilde{x}}$.

4.3 *Uniform Velocity and Electrical Conductivity*

4.3.1 Load with Point Electrode

If the flow discussed in 4.3.1 is suggested with point electrodes and a load current per unit depth I is passed through the circuit, the field distribution shown in Fig. 4-1 results. These results for $B^{(i)}/B_m^{(0)}$ are for a current $\tilde{I} \equiv I/\mu_0^{-1} B_m^{(0)} = 0.25$ and a Reynolds number $R_M = 10$. The convection of the magnetic field down stream by the fluid is considerable and the eddy current cells at the magnetic field edge are as significant as the generator current. The result of Gill [13] is consistent with this computation.

4.3.2 Load with Finite Electrode

If the basic situation above is supplied with finite electrodes, the upstream eddy current cells couple its current into the generator circuit as shown in Fig. 4-2. If the generator current is increased to $\tilde{I} = 1$, the result is shown in Fig. 4-3.

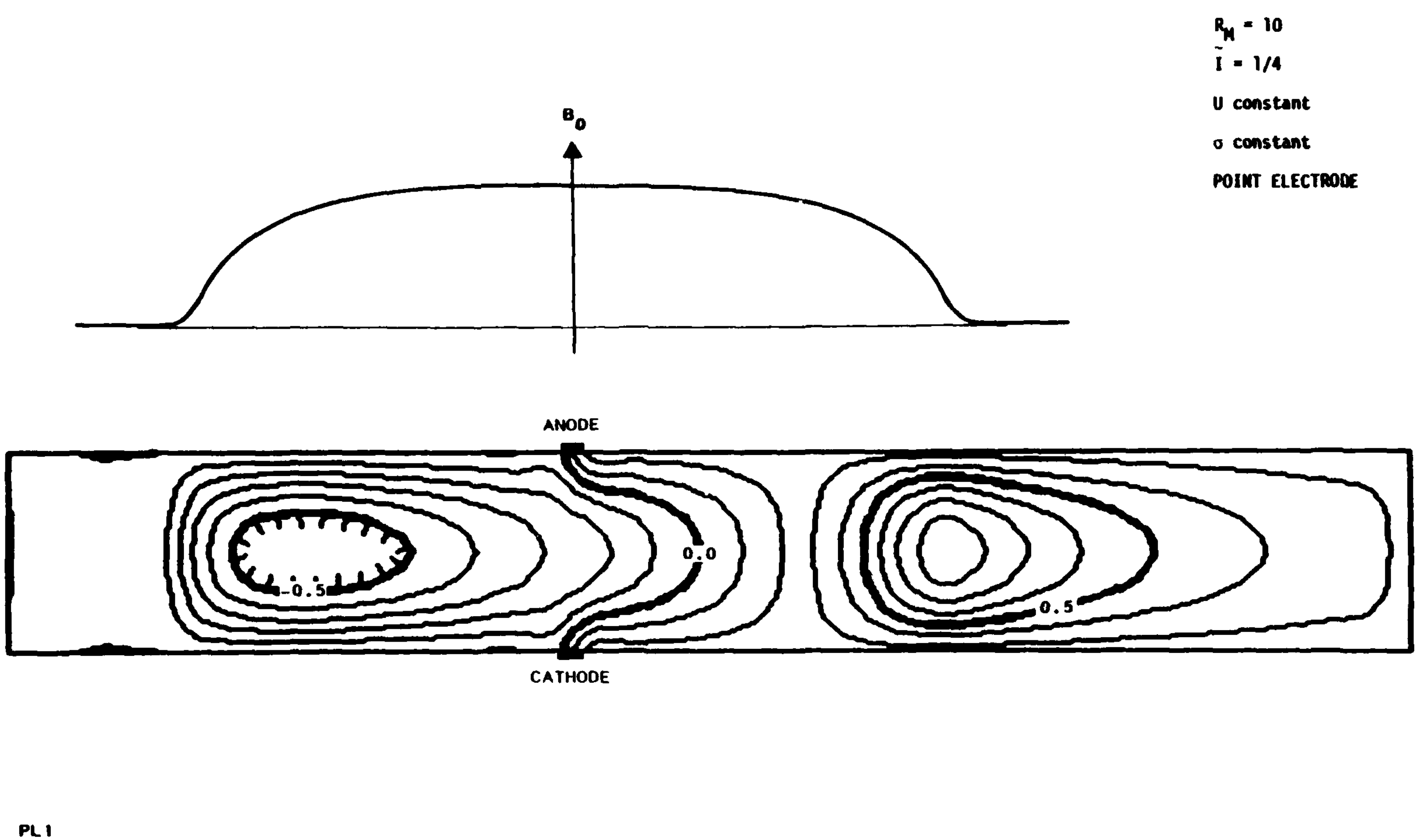

Fig. 4-1. Induced magnetic field isolevels in high magnetic Reynolds number flow. Uniform velocity and conductivity; point electrode

9-3315

STD RESEARCH CORPORATION

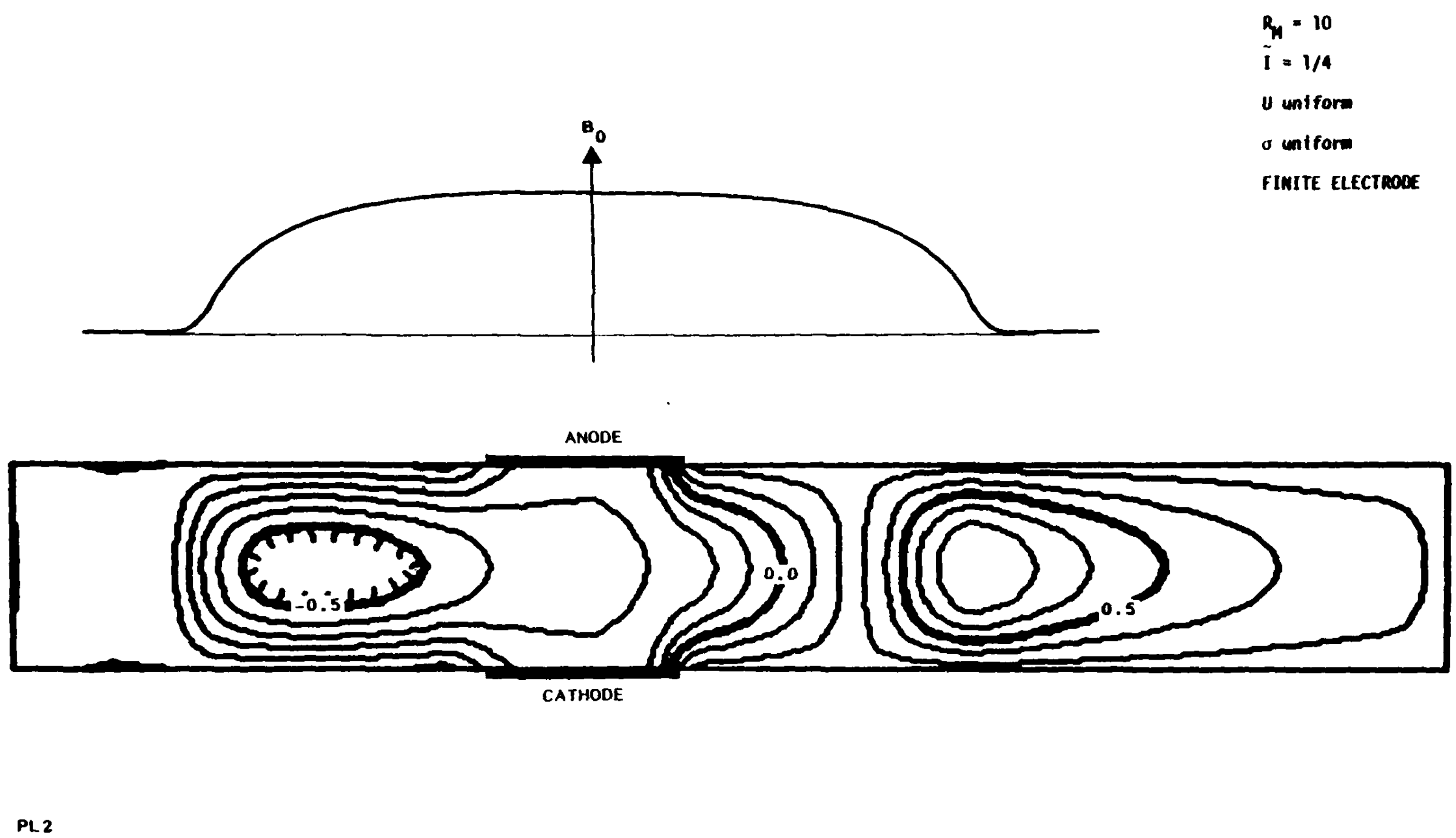

Fig. 4-2. Induced magnetic field isolevels in high magnetic Reynolds number flow. Uniform velocity and conductivity; finite electrode

9-3316

STD RESEARCH CORPORATION

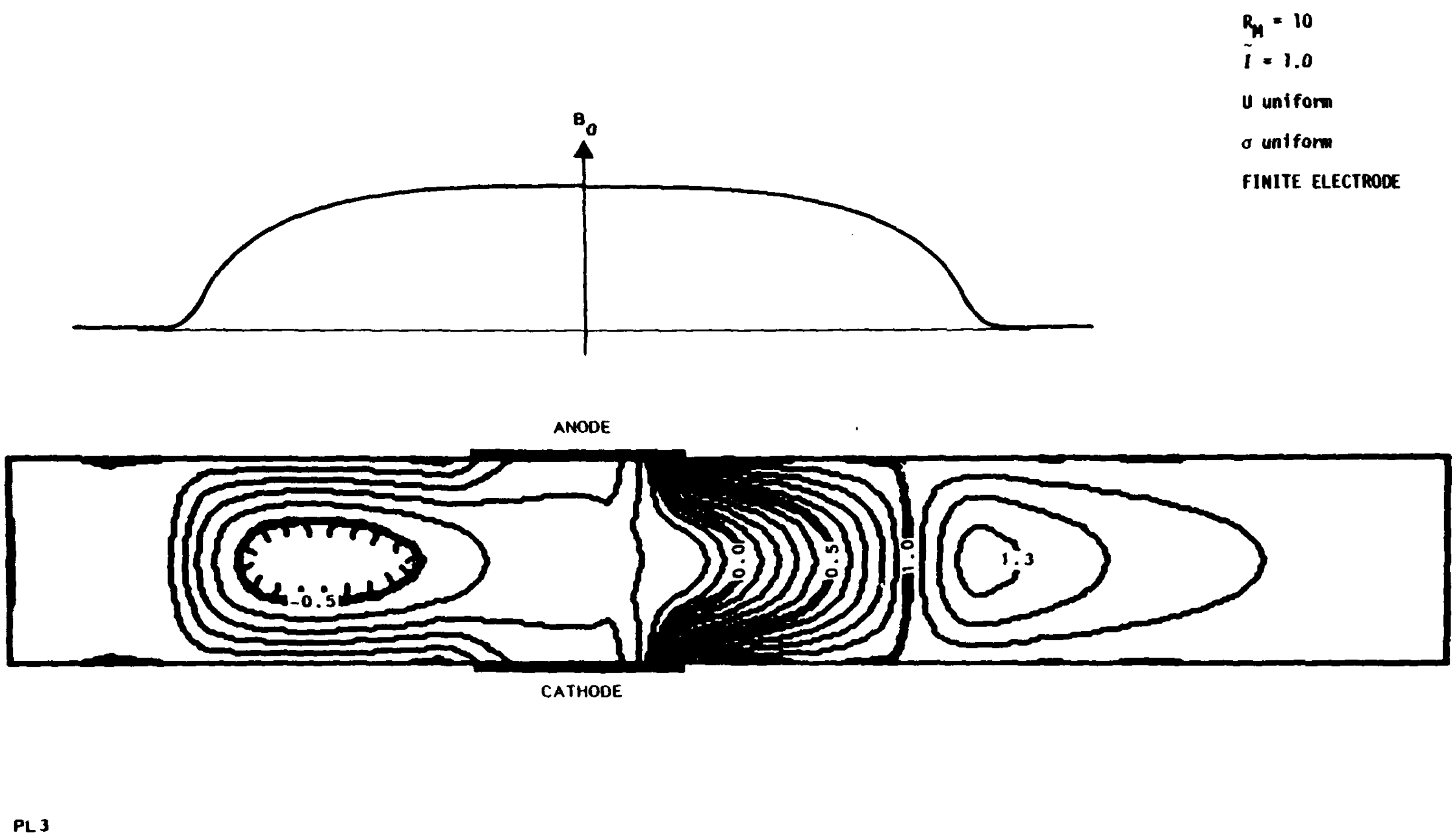

Fig. 4-3. Induced magnetic field isolevels in high magnetic Reynolds number flow. As in Fig. 4-2 but $\tilde{I} = 1$.

9-3317

STD RESEARCH CORPORATION

4.4 Nonuniform Velocity and Conductivity Distributions Resulting from a Shock System

We now consider nonuniformities in electrical conductivity and velocity resulting from an hypothesized oblique shock system. We consider discontinuous distribution across the shock with $(\ )_1$ denoting the upstream side of the shock and $(\ )_2$ denoting the downstream side. The magnetic Reynolds number based upon upstream conditions is $R_{M_0} = 10$ for all cases. The current is $\tilde{I} = 1$ for all cases.

4.4.1 Shock in front of Electrodes

When the shock is in front of the electrodes, the induced field distribution, shown in Figs. 4-4 through 4-6 result. In Fig. 4-4 there is a conductivity group of 3 and no velocity jump. In Fig. 4-5 the conductivity jump is 10 with no velocity jump. In Fig. 4-6, the conductivity jump is 10 and there is a velocity jump of 1/2.

4.4.2 Shock in Channel Center

In Fig. 4-7, the conductivity jump of 10 is shown with the shock system located in the channel center. With the shock further downstream, the front eddy cell is less free to couple into the electrodes and generator circuit.

4.4.3 Shock at Upstream Edge of Magnetic Field

When the shock is moved upstream to the upstream edge of the magnetic field, the electrodes strongly couple the upstream eddy cell.

4.5 Nonuniform Velocity and Conductivity Distributions Resulting from Supersonic Boundary Layers on the Walls of the MHD Generator Duct

4.5.1 Flow Structure for Electrical Interaction

The flow field has been calculated as that resulting from a reservoir which feeds the duct with Argon at an inlet velocity of 10 km/sec,

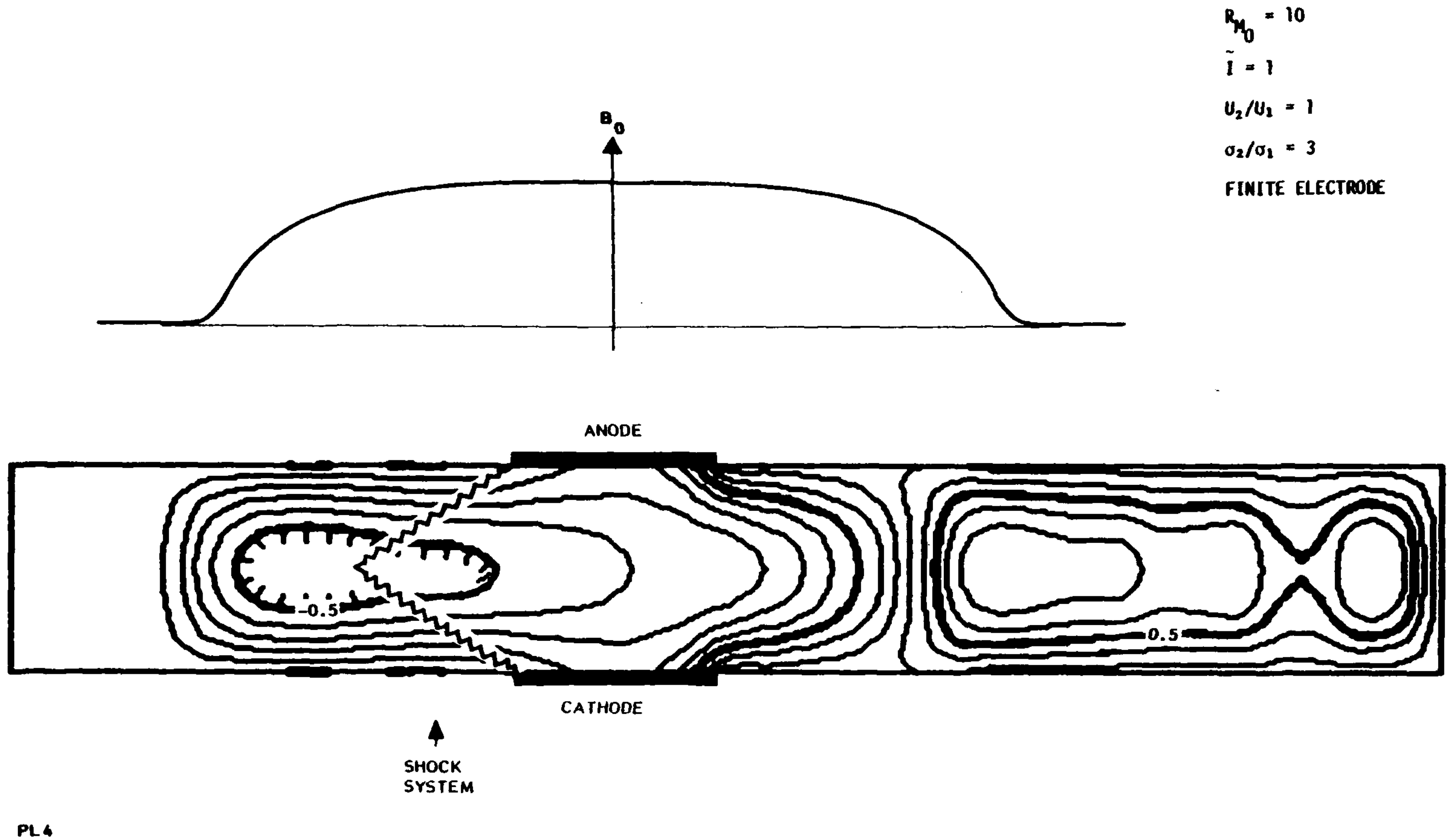

Fig. 4-4. Induced magnetic field isolevels in high magnetic Reynolds number flow. Shock system present with $(\ )_1$ denoting upstream and $(\ )_2$ denoting downstream conditions. Conductivity jump only

9-3318

STD RESEARCH CORPORATION

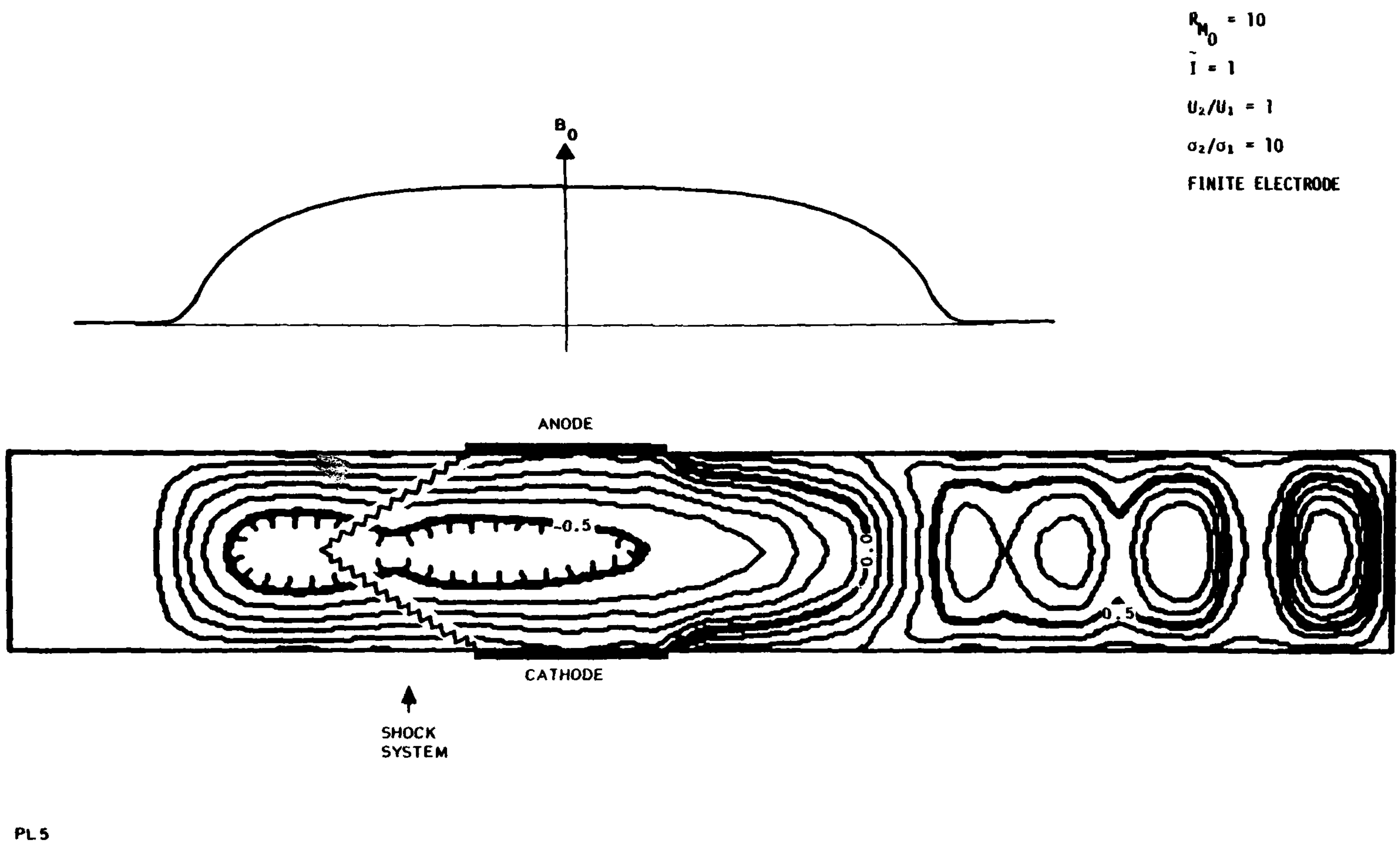

Fig. 4-5. Induced magnetic field isolevels in high magnetic Reynolds number flow. As in Fig. 4-4, but conductivity jump of 10; downstream eddy cell structure influenced by zero current flow boundary condition at duct exit.

9-3319

STD RESEARCH CORPORATION

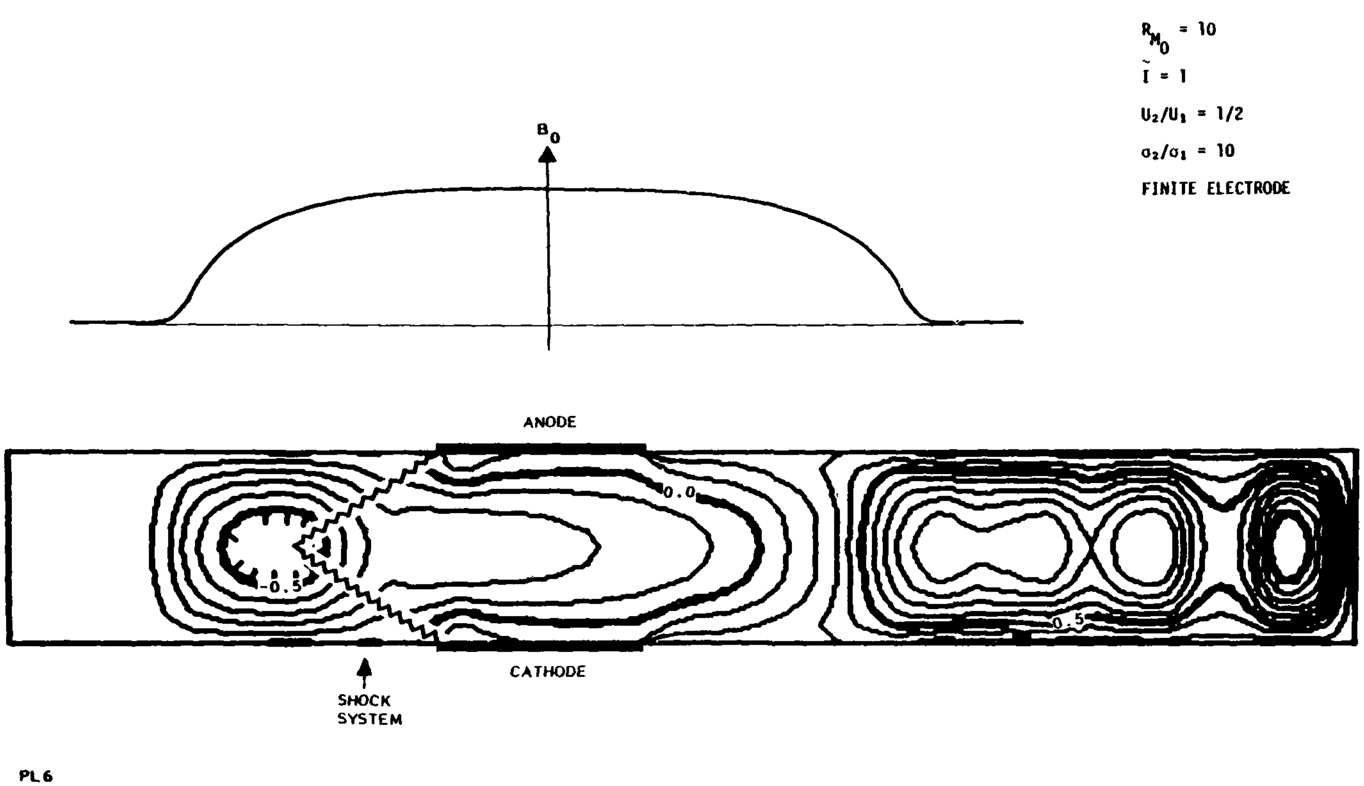

Fig. 4-6. Induced magnetic field isolevels in high magnetic Reynolds number flow. As in Fig. 4-5, but with a velocity jump of 1/2

9-3320

STD RESEARCH CORPORATION

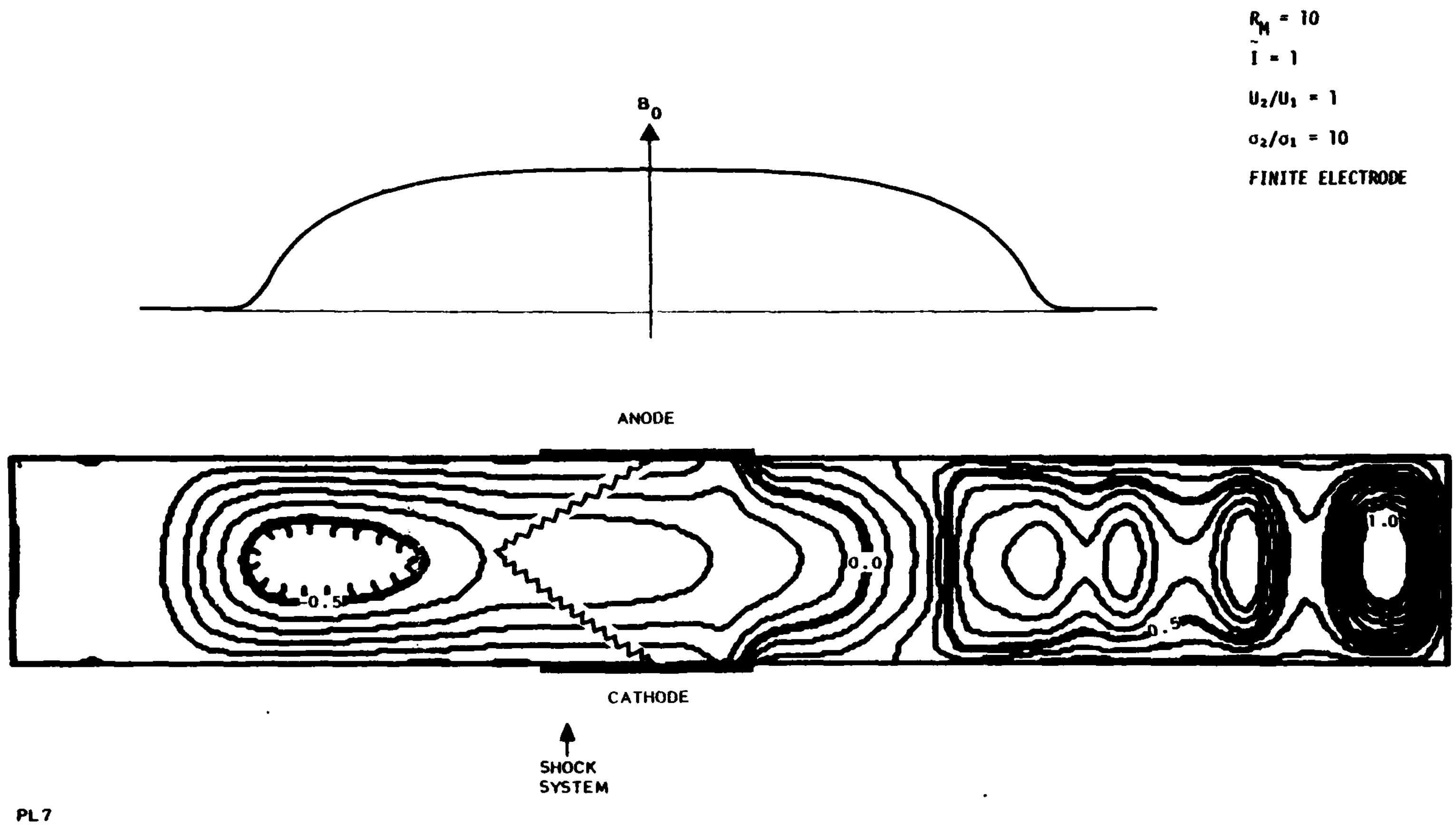

Fig. 4-7. Induced magnetic field isolevels in high magnetic Reynolds number flow. Conductivity jump of 10 and shock system moved into channel center

9-3321

STD RESEARCH CORPORATION

an internal energy of 37 MJ/kg, a pressure of 10 k bar, and a nominal electrical conductivity of 25,000 mho/m at the duct inlet. The resulting turbulent boundary layer interaction is considerable as the flow proceeds down the duct.

The generator electrodes are located at 0.6 m downstream from the duct entry from the driver. At the station 10 cm upstream from the generator inlet (x = 0.50 m) the conditions of the flow are

Velocity at duct centerline	9612 m/sec
Temperature at duct centerline	36,800 K
Mach number	3.14
Boundary layer thickness	5.5 mm

At the center of the generator section, (x = 0.60 m) these values are

Velocity at duct centerline	9520 m/sec
Temperature at duct centerline	36,930 K
Mach number	3.11
Boundary layer thickness	6.5 mm

At the exit of the duct, (x = 0.70 m) these values are

Velocity at duct centerline	9430 m/sec
Temperature at duct centerline	36,970 K
Mach number	3.07
Boundary layer thickness	7.5 mm

This distribution of nonuniform velocity and temperature in x and y (with corresponding density and conductivity nonuniformity) resulting from the boundary layers is used as the basis for the electrical calculations utilizing Eq. (67). The nondimensionalized values are based upon the velocity and conductivity at the duct inlet (x = 0). The Reynolds number is based upon the channel height, h and has the value 7.1.

4.5.2 Electrical Conduction at Vanishing Magnetic Reynolds Number

We first exhibit the nonuniform electrical conduction in the channel at low magnetic Reynolds number, $R_M = 0.01$. The total generator current per unit depth, $\tilde{I}$, has the value 0.01.

The induced magnetic field, $\vec{\tilde{B}}^{(i)}$ nondimensionalized on the maximum value of the applied field is shown in Fig. 4-9 corresponding to the current $\tilde{I}$. It can be seen there is negligible convection of the current distribution; the current spreads out to fill the central portion of the channel. The principal effects of the electrical nonuniformities are the voltage drops through the cool boundary layers and the fringing of the current at the electrode edges.

4.5.3 Electrical Conduction at High Magnetic Reynolds Number

When the magnetic Reynolds number is $R_m = 7.13$ the resulting induced magnetic field, $\tilde{B}^{(i)}$, is shown in Fig. 4-10. For the case of $\tilde{I} = 1$ it can be seen that the generator current is driven downstream in the usual fashion, the bulk of the power actually being produced somewhat downstream of the electrodes. Because of the cool, poorly conducting boundary layers, the eddy-current cells at the magnet edges do not couple into the generator circuit as they do in the cases of Figs. 4-3 through 4-8 which do not include boundary layer effects.

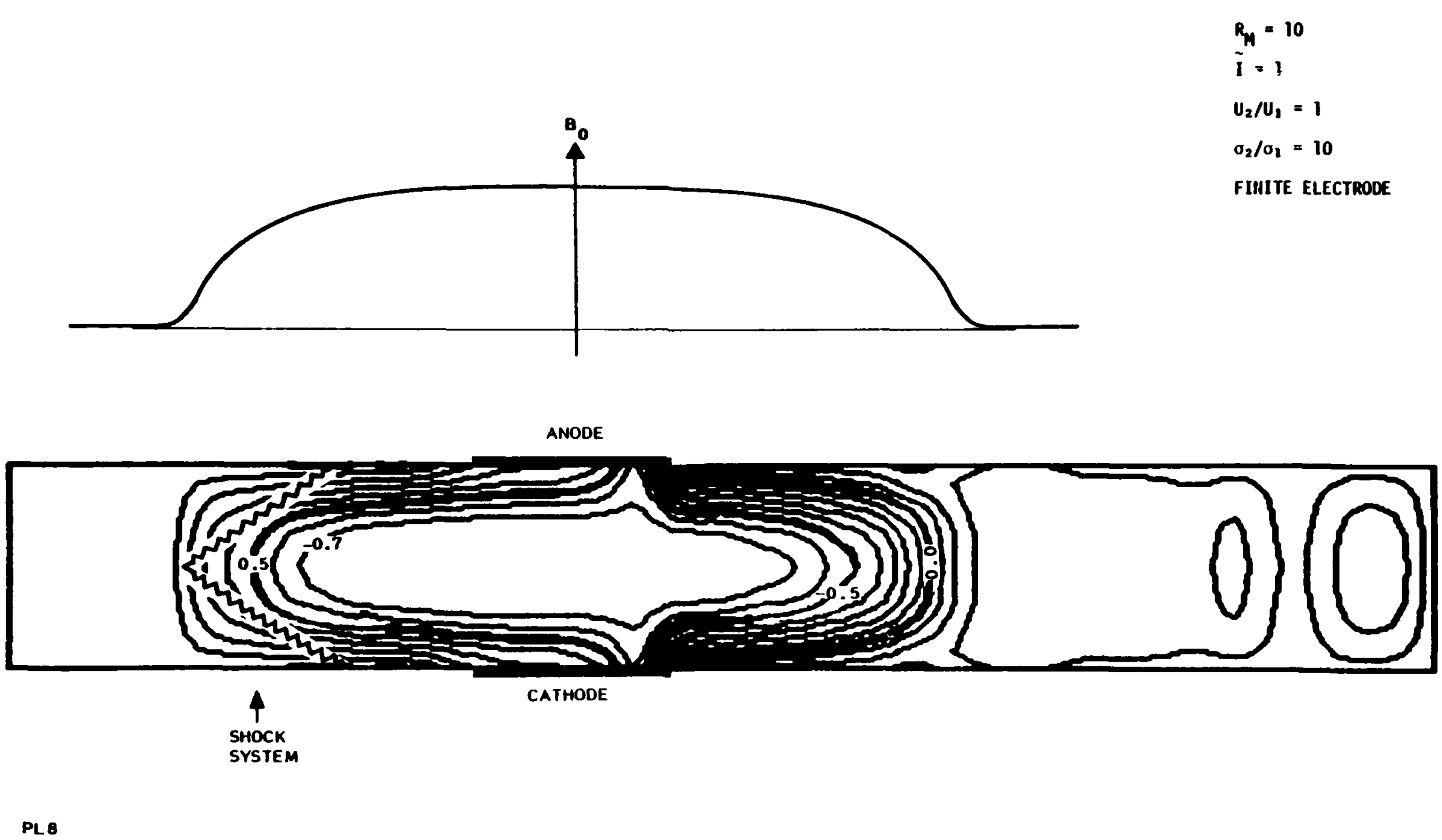

Fig. 4-8. Induced magnetic field isolevels in high magnetic Reynolds number flow. Conductivity jump of 10 and shock system moved upstream to magnetic field edge

9-3322

STD RESEARCH CORPORATION

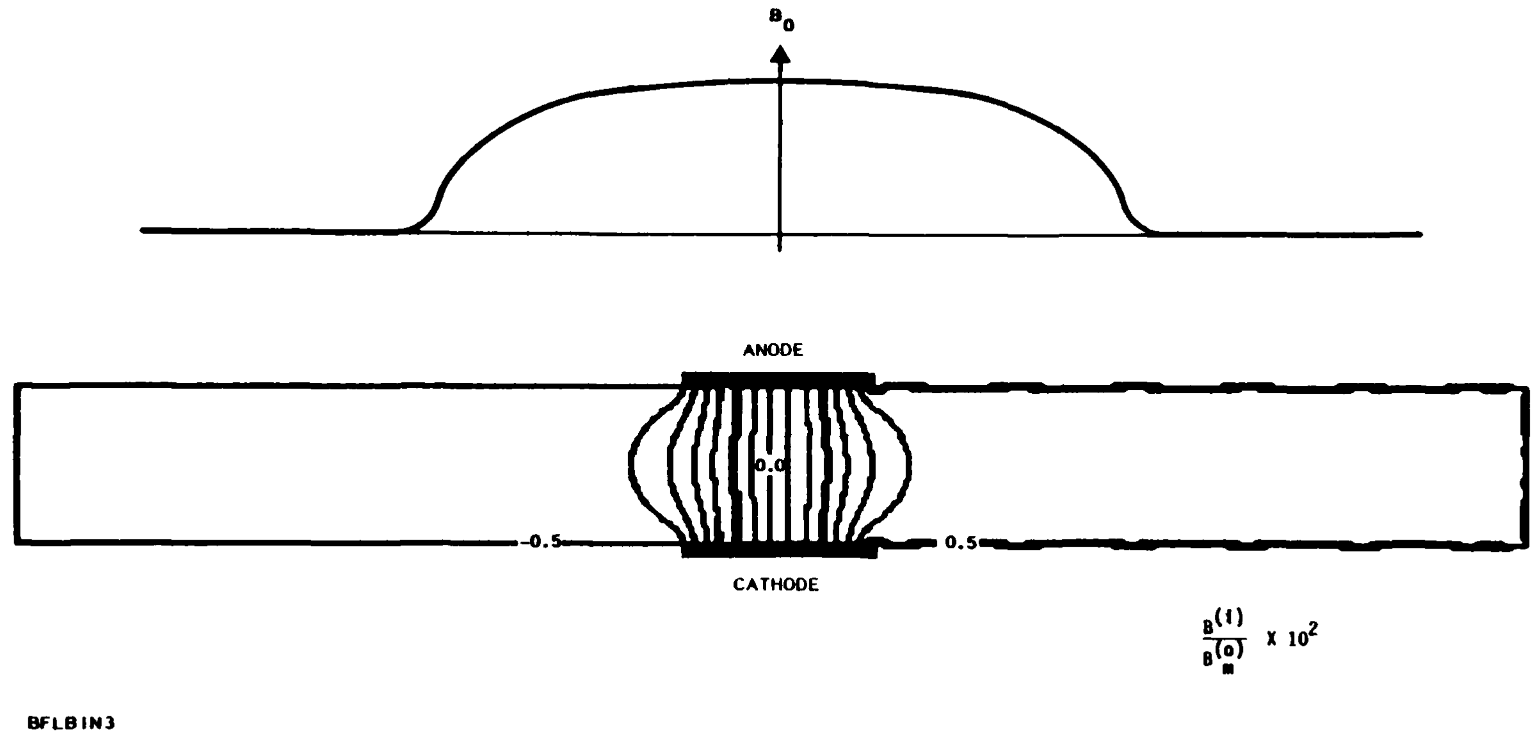

Fig. 4-9. Induced magnetic field isolevels under conditions of low magnetic Reynolds number flow ($R_M = 0.01$) and velocity and conductivity nonuniformities resulting from supersonic boundary layer development through the duct

9-3314

STD RESEARCH CORPORATION

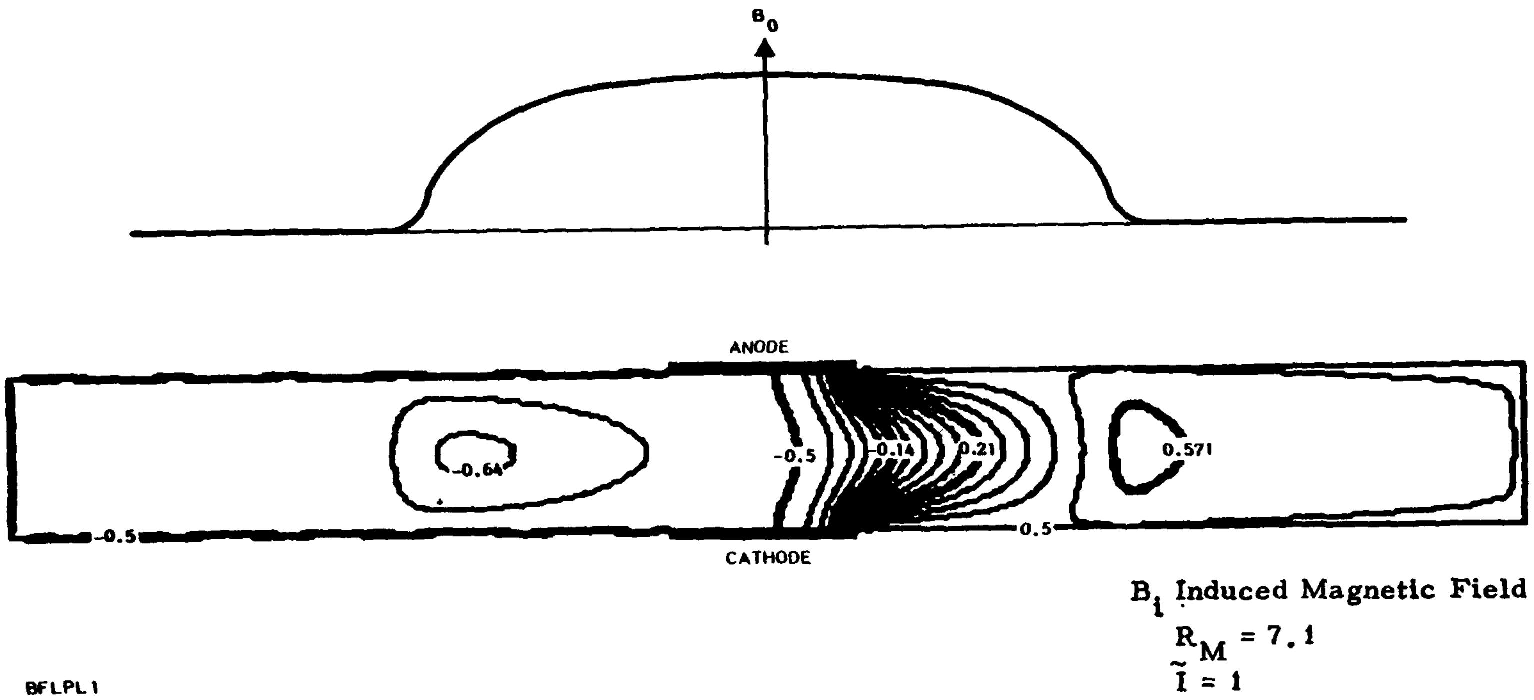

Fig. 4-10. Induced magnetic isolevels for high magnetic Reynolds number flow ($R_M = 7.1$) and velocity and conductivity nonuniformities resulting from supersonic boundary layer development through the duct

9-3312

STD RESEARCH CORPORATION

References

[1] M. Jones, "Explosion Driven Linear MHD Generators," Proc. Conference on Megagauss Magnetic Field Generation by Explosives, Frescati, Italy, Sept. 1965.

[2] I. I. Glass, S. K. Chan, and H. L. Brode, "Strong Planar Shock Waves Generated by Explosively-Driven Spherical Implosions," AIAA J., Vol. 12, No. 3, March 1974, p. 367.

[3] J. Roscieszewski and W. Gallaher, "Shock Tube Flow Interaction with an Electromagnetic Field," Proc. Seventh Int'l. Shock Tube Symp. ed. I. I. Glass, Univ. of Toronto, p. 475-489 (1970).

[4] J. J. Rosceszewski and T. T. Yeh, "Shock Tube Flow Passing Through a Section of a Linear MHD Generator," AIAA J., Vol.11, No.12, p.1756 (1973).

[5] C. K. Chu and Robert A. Gross, "Shock Waves in Plasma Physics," Adv. Pl. Phys. ed. A.Simon and W. B. Thompson, Vol.2, p.139, (1969).

[6] C. K. Chu, "Dynamics of Ionizing Shock Waves: Shocks in Transverse Magnetic Fields," Phys. Fluids, Vol. 7, No.8, p.1349, August 1964.

[7] Dmitri A. Bout and Robert A. Gross, "Interaction of an Ionizing Shock Wave with a Transverse Magnetic Field," Phys. Fluids, Vol.13, No.6, p.1473, June 1970.

[8] Dmitri A. Bout, Richard S. Post and Herman Presby, "Ionizing Shocks Incident Upon a Transverse Magnetic Field," Phys. Fluids, Vol.13, No.5, p. 1399, May 1970.

[9] Ya. B. Zel'dovich and Yu. P. Raizer, Physics of Shock Waves and High Temperature Hydrodynamic Phenomena, Vol. 1, Academic Press, New York, 1966, p. 234-238.

[10] R. F. Warming, et al., "Second- and Third-Order Noncentered Difference Schemes for Nonlinear Hyperbolic Equations," AIAA J., Vol. 11, No. 2, February 1973.

References (cont'd)

[11]. D. A. Oliver, "A Constricted Discharge in Magnetohydrodynamic Plasma," Proc. 15th Symposium on Engineering Aspects of Magnetohydrodynamics, Univ. Pennsylvania, Philadelphia, p. IX.4, May 1976.

[12] S. T. Demetriades, C. D. Maxwell, G. S. Argyropoulos, and G. Fonda-Bonardi, "Influence of Controlled Turbulence on Gaseous Discharges," Proc. 11th Symposium on Engineering Aspects of Magnetohydrodynamics, Caltech, Pasadena, California, p.64, March 1970.

[13] S. P. Gill, D. W. Baum, and H. Calvin, "Explosive MHD Research," Artec Assoc., Annual Rpt. No. 119AR to ONR, April 1975 - April 1976.

ONR PULSED POWER PROGRAM

DISTRIBUTION LIST

Defense Documentation Center (12)
Building 5
Cameron Station
Alexandria, VA 22314

Dr. E. T. Florance
Office of Naval Research Branch Office
1030 East Green Street
Pasadena, CA 91106

Mr. J. A. Satkowski (3)
Office of Naval Research
Code 473
Arlington, VA 22217

Mr. John Siambis
Office of Naval Research
Code 421
Arlington, VA 22217

Naval Research Laboratory (6)
Code 2627
Washington, DC 20375

Naval Research Laboratory (6)
Code 2629
Washington, DC 20375

Dr. P. Turchi
Naval Research Laboratory
Code 6770
Washington, DC 20375

Dr. A. E. Robson
Naval Research Laboratory
Code 6708
Washington, DC 20375

Mr. Franklin R. Smith
Army Corps of Engineers
Code HNDED-SR
P.O. Box 1600
Huntsville, AL 35807

Mr. Robert Dannenburg
NASA Ames Research Center
Code NS229-4
Moffett Field, CA 94035

Dr. David Fenneman
Naval Surface Weapons Center
Code F12
Dahlgren, VA 22448

Dr. T. L. Berger
Naval Surface Weapons Center
Code F12
Dahlgren, VA 22448

Dr. George Ullrich
Headquarters
Defense Nuclear Agency
Washington, DC 20305

Mr. John Farber
Headquarters
Defense Nuclear Agency
Washington, DC 20305

Dr. Terry Godlove
Department of Energy
Code C-404
Washington, DC 20545

Dr. Joseph Mangano
Defense Advanced Research
Projects Agency
Strategic Technology Office
1400 Wilson Boulevard
Arlington, VA 22209

Dr. F. J. Rogers
Lawrence Livermore Laboratory
H - Division
P. O. Box 808
Livermore, CA 94550

Dr. Marvin Ross
Lawrence Livermore Laboratory
H - Division
P. O. Box 808
Livermore, CA 94550

Dr. Richard More
Lawrence Livermore Laboratory
H - Division
P. O. Box 808
Livermore, CA 94550

Dr. Harold Graboske
Lawrence Livermore Laboratory
L 355
P.O. Box 808
Livermore, CA 94550

Dr. Hugh E. DeWitt
Lawrence Livermore Laboratory
P. O. Box 808
Livermore, CA 94550

Dr. William Nellis
Lawrence Livermore Laboratory
L 355
P.O. Box 808
Livermore, CA 94550

Mr. William Cowan
Sandia Laboratories
P.O. Box 4230
Albuquerque, NM 87510

Dr. R. F. Flagg
Physics International
2700 Merced Street
San Leandro, CA 94577

Professor S. Winterberg
University of Nevada
Desert Research Institute
Reno, NV 89507

Dr. M. Kristiansen
Texas Tech University
Department of Electrical Engineering
Lubbock, TX 79409

Dr. Peter Ottenger
Thermo Electron Corporation
101 First Avenue
Waltham, MA 02154

Mr. C. D. Bangerter
STD Corporation
P.O. Box C
Arcadia, CA 91006

Dr. David Oliver
STD Corporation
P.O. Box C
Arcadia, CA 91006

Mr. Thomas F. Swean, Jr.
STD ~~Corporation~~
P.O. Box C
Arcadia, CA 91006

Dr. Dennis W. Baum
Artec Associates, Inc.
26046 Eden Landing Road
Hayward, CA 94545

Dr. Deb Mukherjee
Artec Associates, Inc.
26046 Eden landing Road
Hayward, CA 94545

Dr. Stephen P. Gill
Artec Associates, Inc.
26046 Eden Landing Road
Hayward, CA 94545

Prof. Horst Wilhelm
University of Florida
Department of Engineering Sciences
Gainsville, FL 32611

Dr. B. Zauderer
General Electric Company
Valley Forge Space Center
P.O. Box 8555
Philadelphia, PA 19101

Dr. E. Tate
General Electric Company
Valley Forge Space Center
P.O. Box 8555
Philadelphia, PA 19101

Dr. Jay P. Boris
Naval Research Laboratory
Laboratory for Computational Physics
Code 6020
Washington, DC 20375